ADVANCED MATERIALS
www.advmat.de

Structural Understanding for High-Voltage Stabilization of Lithium Cobalt Oxide

Cong Lin, Jianyuan Li, Zu-Wei Yin,* Weiyuan Huang, Qinghe Zhao, Qingsong Weng, Qiang Liu, Junliang Sun, Guohua Chen,* and Feng Pan**

The rapid development of modern consumer electronics is placing higher demands on the lithium cobalt oxide ($LiCoO_2$; LCO) cathode that powers them. Increasing operating voltage is exclusively effective in boosting LCO capacity and energy density but is inhibited by the innate high-voltage instability of the LCO structure that serves as the foundation and determinant of its electrochemical behavior in lithium-ion batteries. This has stimulated extensive research on LCO structural stabilization. Here, it is focused on the fundamental structural understanding of LCO cathode from long-term studies. Multi-scale structures concerning LCO bulk and surface and various structural issues along with their origins and corresponding stabilization strategies with specific mechanisms are uncovered and elucidated at length, which will certainly deepen and advance the knowledge of LCO structure and further its inherent relationship with electrochemical performance. Based on these understandings, remaining questions and opportunities for future stabilization of the LCO structure are also emphasized.

1. Introduction

The 2019 Nobel Prize in Chemistry-awarded rechargeable lithium-ion batteries (LIBs) are reshaping our modern world into a fossil fuel-free sustainable society, powering not just traditional 3C devices but also the growing electric mobility and grid energy storage.[1] Superior electrochemical performance in terms of capacity and energy density of LIBs is largely pursued nowadays to meet the increasing demands for "mobile living"; however, it is seriously impeded by the bottleneck of cathode materials. This is because the cathode dictates the behavior and quantity of shuttling Li^+ ions and holds the largest percentage in LIBs by both weight and cost.[2] In the contemporary battery community, layered lithium cobalt oxide ($LiCoO_2$, LCO for short) is the most successful and prototype cathode.[3] It was proposed in 1980 by John B. Goodenough et al. with reversible Li^+ deintercalation and intercalation, which for the first time freed the dependence on the unsafe Li metal anode and raised battery working voltage to over 4.0 volt (V; vs Li^+/Li).[4] Then in 1991, LCO was employed to serve the very first commercial LIBs by SONY,[5] and this has greatly boomed the development of LIB technologies and materials.

To date, despite over 40 years since its birth with a variety of alternates like $LiFePO_4$ (LFP), $LiMn_2O_4$ (LMO), Ni-rich ternary $Li[Ni_xCo_y(Al\text{ or }Mn)_{1-x-y}]O_2$ (NCA or NCM), and Li- and Mn-rich layered oxide (LMRO) developed,[6] LCO is still very relevant and extensively applied in major commercial LIBs due to its distinct merits of high working voltage, highly compact density, and consequent high energy density, excellent conductivity, ease of preparation, and mature manufacturing. Although concerns over inelastic supply, unethical mining, and limited reserves leading to high cost make the use of Co controversial,[2] which prompts the battery community to vigorously develop alternates to phase it out, Co and LCO continue to be indispensable to LIBs for the time being.[7] Typically, it is highly challenging to completely eliminate Co from hot-spot Ni-rich NCA and NCM in the near term due to the significance of Co in reinforcing structural stability and conductivity. While LCO may not be a suitable choice for large-scale energy storage batteries because of cost-effectiveness considerations, especially when compared to NCA and NCM for electric vehicles, it remains highly competitive in terms of energy density.[8] For example, upon a cut-off voltage of 4.4 V, LCO delivers a volumetric energy density of 2812 Wh L^{-1} while NCM811 ($LiNi_{0.80}Co_{0.10}Mn_{0.10}O_2$) offers ≈2600 Wh L^{-1} and NCA ($LiNi_{0.80}Co_{0.15}Mn_{0.05}O_2$) ≈2700 Wh L^{-1}.[9] Furthermore, LCO does have unique and specific application scenarios of its

C. Lin, J. Li, Z.-W. Yin, W. Huang, Q. Zhao, F. Pan
School of Advanced Materials
Peking University Shenzhen Graduate School
Shenzhen 518055, China
E-mail: lincong@pku.edu.cn; yinzuwei@xmu.edu.cn; panfeng@pkusz.edu.cn

C. Lin, Q. Weng, Q. Liu, G. Chen
Department of Mechanical Engineering
The Hong Kong Polytechnic University
Kowloon, Hong Kong SAR 999077, China
E-mail: guohua.chen@polyu.edu.hk

C. Lin
Department of Applied Biology and Chemical Technology
The Hong Kong Polytechnic University
Kowloon, Hong Kong SAR 999077, China

C. Lin, J. Li, J. Sun
College of Chemistry and Chemical Engineering
Peking University
Beijing 100871, China

The ORCID identification number(s) for the author(s) of this article can be found under https://doi.org/10.1002/adma.202307404

DOI: 10.1002/adma.202307404

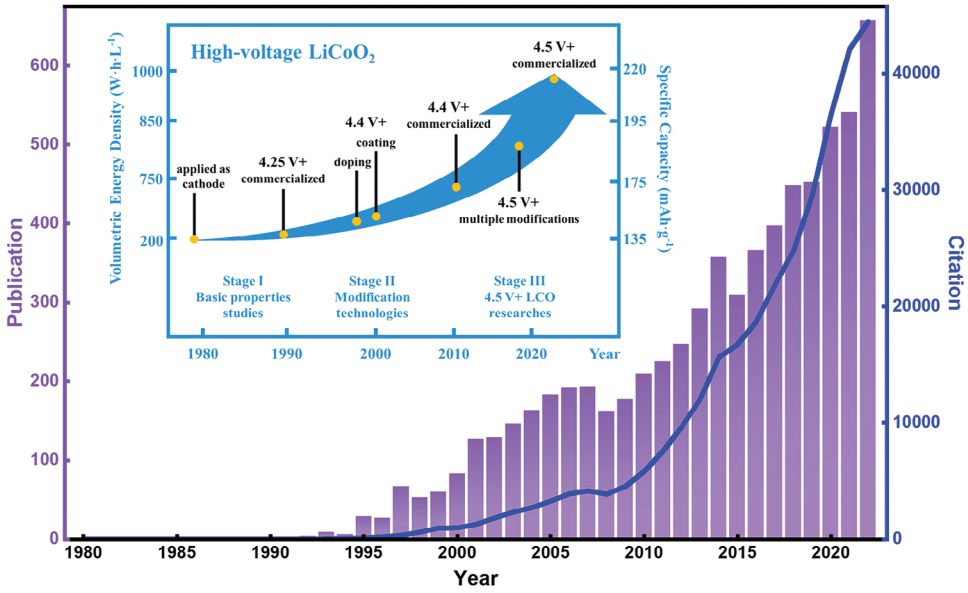

Figure 1. Distribution of publication and citation of LCO study by year. From Web of Science as of September 20th, 2023, with "$LiCoO_2$" and "battery" as the search topic.[11] Inset showing the development of H-LCO. Reproduced with permission.[12] Copyright 2020, Elsevier.

own. Particularly in the consumer electronics market where a high volumetric energy density is mandatory, LCO is and will continue being the monopoly of the cathode in the foreseeable future, which has also become the model material for exploring advanced battery technologies like solid-state electrolyte (SSE) and fast charging.[10] Most importantly, LCO still has a huge potential for higher capacity and energy density and has thus attracted tremendous research interest over the last two decades (**Figure 1**). Such a pursuit is known as the exploitation of the so-called high-voltage LCO (H-LCO), as LCO is a voltage-limiting cathode whose capacity and energy density are restricted by operating voltage (**Table 1**).[9b] Specifically, according to $\Delta E = \int_0^{\Delta Q} V \times qdq$ (E, V, and q stand for energy density, operating voltage, and capacity, respectively) to quantify electrochemical performance, LCO capacity and energy density can be simultaneously boosted by simply increasing operating voltage. Unfortunately, this is critically subject to the intrinsic high-voltage instability of LCO structure regarding both bulk phase and surface, with well-known structural issues like irreversible phase transitions accompanied by twin boundaries and layer gliding, interfacial side reactions, oxygen redox, and so on. These not only deteriorate LCO electrochemical performance with increased impedance and rapid decay in available capacity, discharge voltage, rate capability, and cyclic life but also pose safety risks, such as heat release, electrolyte leakage, and battery swelling due to destructive and excessive side reactions.

Table 1. Electrochemical performance of LCO at different cut-off voltages. Reproduced with permission.[9b] Copyright 2018, Elsevier.

Voltage	4.2 V	4.3 V	4.4 V	4.5 V	4.6 V
Capacity (mA h g^{-1})	140	155	170	185	220
Average voltage (V)	3.91	3.92	3.94	3.97	4.03
Specific energy (Wh kg^{-1})	547.3	607.6	669.6	733.5	885.9
Specific energy (Wh L^{-1})	2299	2552	2812	3081	3721
Increment of energy density		11%	10%	9.5%	21%

With the goal of stably approaching theoretical capacity, achieving H-LCO is essentially the structural stabilization at high voltages, which is the driving force for decades of LCO development (inset in Figure 1).[12] In early studies, fundamentals of LCO structure and property, especially the structural understandings regarding its bulk and surface during the electrochemical process, were the focus. It was found that LCO underwent a series of phase transitions upon high cut-off voltages, leading to gradual deterioration of structure and electrochemical performance. This is the main reason why the first commercial LIBs were cycled below 4.2 V with only half of LCO theoretical capacity (≈140 mA h g^{-1}; theoretical value: 274 mA h g^{-1}). Nonetheless, the structural knowledge obtained then is of considerable significance even today and greatly promotes subsequent progress. Following that, research aiming at improving LCO structural stability was vastly conducted, and various modification strategies, mainly elemental doping and surface coating, have been developed.[3] These facilitated the stable cycling of LCO at a cut-off voltage of 4.4 V and enabled the second-generation LCO-based commercial LIBs with a capacity of ≈170 mA h g^{-1}.[13] Currently, massive efforts are being invested to realize H-LCO with a much larger capacity at higher voltages (e.g., ≈220 mA h g^{-1} at 4.6 V cut-off voltage) using a range of modifications, including not only elemental doping and surface coating but also combined modifications on others like electrolytes, additives, binders, etc. This imposes big challenges for high-voltage stabilization of the LCO structure.

To develop and utilize H-LCO more effectively and rationally, a thorough and precise understanding of LCO structure is

becoming a must. However, there has been no systematic review exclusive on this topic, despite several summaries on LCO electrochemical performance and modifications.[3,14] This review is dedicated to the fundamental understanding of LCO structures. The crystal and electronic structures of LCO are introduced in the beginning, which are the recognized basis of its electrochemistry in LIBs. Various structural issues arising from the electrochemical process are then discussed in depth, followed by structural stabilization to further deepen our knowledge of the LCO structure–performance relationship. In the end, an outlook of remaining issues and potential opportunities is provided for future LCO structural study and H-LCO exploitation.

2. Structural Fundamentals

2.1. Crystal Structure

LCO crystallography was revealed by powder X-ray diffraction (PXRD) in 1958 when there was a common interest in layered transition metal (TM) oxides.[15] LCO possesses an α-$NaFeO_2$-type layered structure with $R\bar{3}m$ space group and unit-cell parameters of a = 2.816(2) Å and c = 14.08(1) Å. According to Pauling's first rule, since the ionic radius ratio of $r(Li^+)$:$r(O^{2-})$ (0.76 Å : 1.40 Å = 0.543) is larger than the minimum value of 0.414 allowed for stable octahedral coordination while smaller than the minimum 0.732 for a cubic arrangement, Li^+ in LCO stably occupies the octahedral voids of anionic oxygen framework. However, the ionic radius ratio of $r(Co^{3+})$:$r(O^{2-})$ (0.545 Å : 1.40 Å = 0.390) is slightly smaller than 0.414 but Co^{3+} virtually adopts octahedral coordination with O^{2-} in LCO, indicating the intrinsic metastability of LCO structure. Specifically, O in LCO is residing at 6*c* site in a cubic closed-packed (ccp) pattern, and Li and Co are orderly arranged at 3*b* and 3*a* sites in the (111) plane and coordinate with O to form edge-shared LiO_6 and CoO_6 octahedra, respectively. All Co—O bonds in CoO_6 octahedra are of equal length yet the O—Co—O angles deviate slightly from those in a perfect octahedron, thereby leading to minor distortion, while the same is true in LiO_6 octahedra. Given ordered cationic arrangement and thermodynamic stability, LCO is one of the rock-salt oxide superstructures. Besides, LCO can be viewed as constructed by three CoO_2 layers stacking along the *c*-axis in the unit cell, with Li^+ ionically bound in the van der Waals gaps of O^{2-} (**Figure 2a**). Based on the notation by Delmas et al.,[16] LCO is an O3-type layered oxide; here "O" indicates the octahedral coordination of interlayer alkali metal (AM; Li in LCO) ions with surrounding O^{2-} while "3" represents the "ABCABC" stacking pattern of O^{2-} layers along *c*-axis or the number of TMO_2 layer in the unit cell. The theoretical density of LCO calculated from its crystal structure is ≈5.05 g cm^{-3} and the compact density for practical applications can reach ≈4.2 g cm^{-3} thanks to its high thermal stability (up to 1000 °C) and low formation energy (predicted value: −1.753 eV $atom^{-1}$) leading to easy synthesis of large crystallites (≈10 µm).[14a] This is the largest among various cathodes, giving LCO a superior volumetric energy density required for consumer electronics.

In addition to O3, LCO also adopts O2- and O4-type layered structures. They cannot be obtained by direct calcination but through Li/Na ion exchange from layered sodic precursors, resulting in non-stoichiometric formulae with Li deficiency.[18] Besides, LCO has a low-temperature $Li_2Co_2O_4$ form with a spinel structure.[19] However, compared to O3, these variants undergo more complicated phase changes with higher structural instability and worse battery performance. This review does not involve these kinds and focuses on O3-type LCO.

2.2. Electronic Structure

Co is trivalent (Co^{3+}) in LCO and situated in the octahedral environment formed by O. According to crystal field theory,[20] Co^{3+} splits its degenerate 3*d* orbitals into three low-energy t_{2g} (d_{xy}, d_{yz}, and d_{xz}) and two high-energy e_g ($d_{x^2-y^2}$ and d_{z^2}) states with separation energy of Δ_O (i.e., octahedral ligand-field splitting energy) (Figure 2b). All six 3*d* electrons of Co^{3+} populate the t_{2g} orbitals and are preferentially paired up (d_{xy}^2, d_{yz}^2, and d_{xz}^2). This results in the low-spin (LS) electronic configuration of Co^{3+} ($3d^6$: $t_{2g}^6 e_g^0$) with minimized unpaired electrons (none in this case), further inducing the non-magnetic feature of LCO. Since the energy in electronic levels of Li is greatly higher than that of Co and O, Li does not mix its electronic states with those of Co and O. Therefore, the electronic structure of LCO is mostly dictated by the CoO_2 complex, especially the Co 3*d* and O 2*p* states with spatial overlap and energetic similarity.[21] Figure 2c depicts the more complete molecular orbital (MO) diagram. Specifically, covalent hybridization of σ overlapping between Co^{3+} 3*d*: e_g and O^{2-} 2*p* occurs and leads to the e_g and e_g^* orbitals, while Co^{3+} 4*s* and 4*p* are hybridized with O^{2-} 2*p* to induce the orbitals of a_{1g} and a_{1g}^*, and t_{1u} and t_{1u}^*, respectively.[22] The t_{2g} states of Co^{3+} 3*d* are shown as the non-bonding orbitals though they actually form some π hybridization with O^{2-} 2*p*.[23] These hybridized orbitals of LCO, including e_g^*, t_{2g}, e_g, t_{1u}, and a_{1g}, can be visualized more intuitively from the band structure calculated using density functional theory (DFT), while the density of states also explicitly show the hybridization between Co^{3+} 3*d* and O^{2-} 2*p* states (Figure 2d).[17] Hence, the bonding orbitals of e_g, a_{1g}, and t_{1u} are governed by O^{2-} 2*p* states due to the lower energy level with strong bonding character, while the antibonding e_g^*, a_{1g}^*, and t_{1u}^* as well as the non-bonding t_{2g} orbitals by Co^{3+} 3*d* states. Besides, these electronic states of Co^{3+}: e_g^{*0} and Co^{3+}: t_{2g}^6 hybridized with O^{2-} 2*p* constitute LCO valence and conduct band, respectively, with the Fermi level positioned between them. The energy gap (E_g) of LCO was measured to be 2.7 eV, indicating a wide-gap semiconductor.[24] Furthermore, the σ overlap of Co^{3+} 3*d* and O^{2-} 2*p* states in an octahedral environment induces a strong interaction between Co^{3+} and O^{2-}, which causes a short Co—O bond length (≈1.92 Å) with a mixed ground state and makes LCO highly covalent and structurally rigid with high elastic/shear modulus, hardness, and Poisson's ratio.[25] This also lowers the migration barrier of Li^+ and promotes fast 2D Li^+ diffusion that follows a tetrahedral-site hop mechanism, that is, from one octahedral site to another through a tetrahedral intermediate. The relatively short Co–Co distance from orderly arranged Co^{3+} and minor defects like Co^{4+} in preparation endow LCO with excellent electronic conductivity, which contributes to remarkable rate capability with favorable Li^+ conductivity.[12]

Comparing electronic configurations of Co^{3+} ($3d^6$: $t_{2g}^6 e_g^0$), Ni^{3+} ($3d^7$: $t_{2g}^6 e_g^1$), and Mn^{3+} ($3d^4$: $t_{2g}^3 e_g^1$) in common layered cathodes,

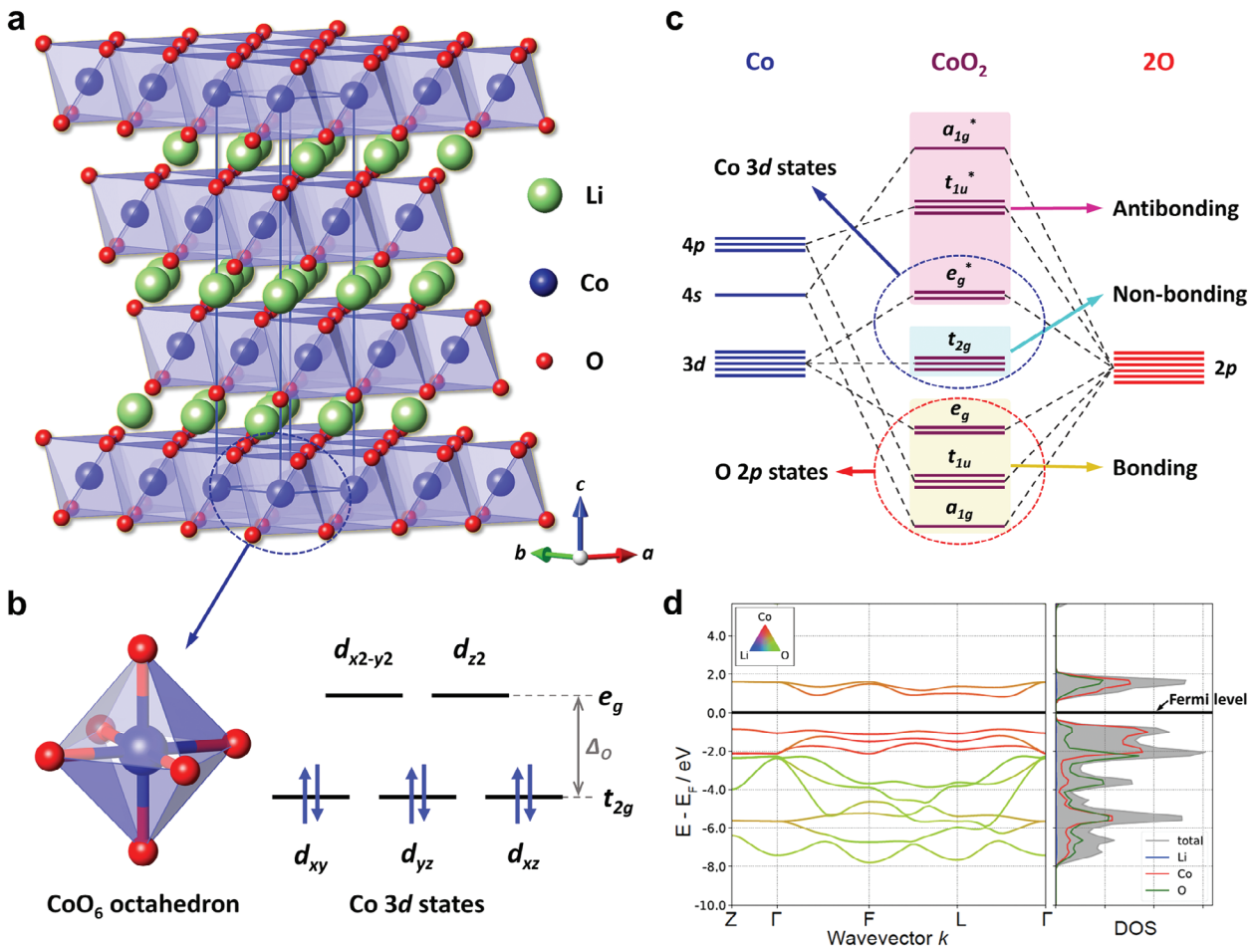

Figure 2. Crystal and electronic structures of LCO. a) Layered structure with blue frame defining unit cell. b) CoO_6 octahedron and schematic electronic configuration of Co^{3+} 3*d* states. c) Molecular orbital diagram for CoO_2 in an octahedral environment. d) Calculated band structure and density of states with projections onto local orbitals. Adapted with permission.[17] Copyright 2021, MDPI.

Co^{3+} is the most stable. Co^{3+}/Co^{4+} redox pair has a lower energy level than Ni^{3+}/Ni^{4+} and Mn^{3+}/Mn^{4+} because the redox-related *d* electron is in t_{2g} band for Co but e_g for Ni and Mn. This enables a higher redox potential of Co^{3+}/Co^{4+} than Ni^{3+}/Ni^{4+} and Mn^{3+}/Mn^{4+} so that LCO exhibits a larger operating voltage than other layered cathodes comprising Ni and Mn.[13] Besides, due to the absence of unpaired electrons in the e_g band, Co^{3+} suffers from less severe Jahn–Teller distortion than Ni^{3+} and Mn^{3+}. Furthermore, as LS Co^{3+} is non-magnetic, no magnetic frustration exists between adjacent Co^{3+} in the triangle lattice of TM layers in LCO, in contrast to Ni-rich NCA and NCM with an unstable higher-energy state due to the magnetic Ni^{3+}.[26] These electronic structural fundamentals imply that LCO possesses higher structural stability than other layered oxides.

3. Structural Instability

As electrochemical charge and discharge (corresponding delithiation and lithiation) proceed, LCO undergoes solid–solution reactions that can be simply summarized as $LiCo^{3+}O_2 \rightleftharpoons Li_xCo^{3+}{}_xCo^{4+}{}_{1-x}O_2 + (1-x)Li^+ + (1-x)e^-$, where "$1-x$" defines delithiation/lithiation molar amount. However, the actual cathodic process is far more complex than what this straightforward chemical equation suggests, as various structural changes arise and evolve at different scales and dimensions. This includes crystal and electronic structures regarding bulk and surface, and their variations badly degrade structural stability and, therefore, electrochemical performance.

3.1. Bulk Structure

The bulk structure beneath the surface region of LCO particles is the main body of Li^+ storage, which determines overall structural stability and electrochemical behavior. Under external electric fields, Li^+ migrates in the LCO bulk lattice, triggering structural strain and further phase transitions and local structural changes. This is a major hurdle for H-LCO and becomes more severe at high voltages.

3.1.1. Phase Evolution

Early studies indicated that Li^+ extraction and insertion in the LCO lattice induce a series of bulk phase transitions.[27] These

are determined almost unambiguously by mainly in situ PXRD (**Figure 3a**) in assistance with others like differential capacity/voltage (dQ/dV) analyses (inset of Figure 3b) and theoretical studies. Figure 3b illustrates the phases and their *c*- and *a*-axis length variations as they evolve with Li^+ concentration (x in Li_xCoO_2). Briefly, there are five phase transitions associating six structures, namely four O3 (H1, H2, M1, and H3; "H" and "M" represent "hexagonal" and "monoclinic", respectively), H1-3, and O1, during high-voltage electrochemical cycles (e.g., >4.7 V; Figure 3c). Following is the detailed phase evolution of LCO during charge.

Pristine O3 LCO is also referred to as H1 or O3 I phase. At the beginning of charge ($0.94 \leq x \leq 1.00$), minor Li^+ extraction leads to AM vacancies and high-spin (HS) paramagnetic Co^{4+}, which possesses $3d^5$: $t_{2g}{}^3e_g{}^2$ electronic configuration with maximized unpaired electrons (five in this case) due to its five 3*d* electrons preferentially occupying all 3*d* orbitals. This increases conductivity with decreased Seebeck coefficient,[30] while H1 is maintained as a solid solution with disordered Li^+/vacancy. The first phase transition from H1 to H2 (or O3 II phase) then occurs at ≈3.92 V when ≈0.06 Li^+ is extracted, and H1/H2 biphase exists upon further delithiation ($0.78 \leq x \leq 0.94$) with a metallic character. This transition does not involve structural changes, although the *c*- and *a*-axis length is becoming larger and smaller due to increased electrostatic repulsion between CoO_2 layers and oxidation of Co^{3+} to smaller Co^{4+}, respectively. H1/H2 phase transition is identified as a strong first-order insulator–metal transition as a Mott transition of impurities, attributed to the electron delocalization within CoO_2 layers and suggested by ^{7}Li magic-angle spinning (MAS) nuclear magnetic resonance (NMR), magnetic measurements, and theoretical calculations.[31] Recent work using in situ Raman and advanced optical tracking of ion dynamics confirmed again H1/H2 transition and biphase.[32] Besides, an intermediate, H2a, has been found in a small x range between H1 and H2 and is presumably related to charge rate (i.e., current density).[33] As the charge proceeds ($0.53 \leq x \leq 0.78$), H1/H2 biphase vanishes to single H2 with linearly increased *c*-axis length and return of HS Co^{4+} to LS Co^{4+} ($3d^5$: $t_{2g}{}^5e_g{}^0$) driven possibly by a unit-cell volume effect.[25a] The vacancies and residual Li^+ are disorderly distributed in AM layers from the start of charge to H2 ($0.53 \leq x < 1.00$).

At ≈4.08 V, half Li^+ is extracted ($x \approx 0.53$) with average Co valence rising to +3.5 (equal amount of Co^{3+} and Co^{4+}) and LCO experiences lattice distortion and a tendency of charge delocalization and energy minimization. This drives Li^+/vacancy ordering and results in H2 transitioning to M1 with threefold symmetry loss. Such a transition has been well validated by in situ PXRD with peak splitting, cyclic voltammetry (CV), and theoretical calculations, and the unit cell of M1 is indexed as $a = 4.90$ Å, $b = 2.81$ Å, $c = 5.05$ Å, and $\beta = 108.3°$ with the $C2/m$ space group.[34] The hexagonal and monoclinic unit cells can be converted as follows: $a_M = \sqrt{3}\ a_H$, $b_M = a_H$, $c_M = (c_H/3)\sin(\beta_M)$, and $\beta_M = 180° - \tan^{-1}[c_H/(\sqrt{3}a_H)]$. The in-plane ordering of alternating Li^+/vacancy was later revealed by electron diffraction (ED) and the space group of M1 was rectified to $P2/m$ for unique Li^+ site, with Li, Co, and O occupying 1*a*, 1*g*, and 1*f*, and 2*m* and 2*n* sites, respectively.[35] This was further verified by single-crystal X-ray diffraction (SCXRD) and direct observation of annular bright field-scanning transmission electron microscopy (STEM).[36] M1 has the largest *c*-axis and smallest *a*-axis throughout charge and discharge, possibly due to the electrostatic balance of attraction and repulsion between and within CoO_2 layers, respectively, implying anisotropic lattice strain and build-up stress. M1 may be more unstable than the spinel phase, as it tends to decompose at a low temperature from transmission electron microscopy (TEM).[37] M1 is maintained with further delithiation ($0.46 \leq x \leq 0.53$) and then transforms back to a hexagonal solid solution known as H3 at ≈4.18 V due to the reappearance of Li^+/vacancy disordering. Comparing H1, H2, M1, and H3, despite the changes in unit-cell parameters and Li content, the stacking pattern of CoO_2 layers remains unchanged, indicating the retention of the O3-type structure without layer gliding and sound reversibility between these phases.

Although H3 exists on further charge ($0.25 \leq x \leq 0.46$), the decrease of the *c*-axis is accelerated, aggravating structural instability with strain and stress. At ≈4.55 V, a second biphase emerges with a phase transition from H3 to another, which had been somewhat controversial. This phase was first observed from in situ PXRD and assigned as the second monoclinic phase, M2; however, its exact structure was not thoroughly known despite only unit-cell parameters without a specific space group.[27b] Some studies reported another phase following H3 but it could not be indexed to the so-called M2.[33,38] Progressively, it was found that this phase should originate from a $CdCl_2$-type hexagonal structure while Ceder et al. proposed a hexagonal phase, H1-3, at low Li concentration from first-principle calculations.[39] H1-3 was later validated by Rietveld refinement against ex situ PXRD, yielding a unit cell of $a = 2.819$ Å and $c = 27.035$ Å with $R\bar{3}m$ space group,[40] whereas some also suggested that H1-3 might be a combination of H3 and M2.[3b] Hence, the H3/H1-3 phase transition is finalized and widely accepted nowadays. H1-3 is a hybrid phase with structural features of O3 and O1 (end member of LCO charge), where Li is located at the 3*a* site while Co and two O at three 6*c* sites. H1-3 adopts a complex O-layer stacking pattern of "ABABCACABCBC", and Li^+ is selectively segregated to every other AM layer while leaving the rest vacant, making six CoO_2 layers in the unit cell. This indicates delithiation inhomogeneity from O3-type H3 to H1-3 with resulting structural strain. In the H3/H1-3 biphase region ($0.12 \leq x \leq 0.25$) with continuous delithiation, the converted *c*-axis length decreases sharply with deteriorative structural instability, which is the major bottleneck for current H-LCO.

As deep delithiation proceeds, H3 disappears and H1-3 solely persists in $0.06 \leq x \leq 0.12$. The last phase transition from H1-3 to O1 occurs at ≈4.64 V, and H1-3 coexists with O1 until the state of charge (SOC) reaches 100%. Despite monoclinic distortion, O1 has a CdI_2-type hexagonal structure with $P\bar{3}m1$ space group and a unit cell of $a = 2.822$ Å and $c = 4.293$ Å.[27b] O1 is Li-free with the chemical formula CoO_2, where Co and O occupy respective 1*a* and 2*d* sites while O layers are "ABAB" stacked along the *c*-axis with one CoO_2 layer in the unit cell. O1 is very unstable due to highly active Co^{4+} and shortened interlayer O–O distance associated with electron–hole chemistry, which transforms to β-$Co(OH)_2$ upon exposure to the atmosphere. Besides, the H1-3/O1 phase transition may be more complicated, as an unknow intermediate has been observed.[41] Compared to other transitions, H1-3/O1 exhibits the largest lattice strain and thus

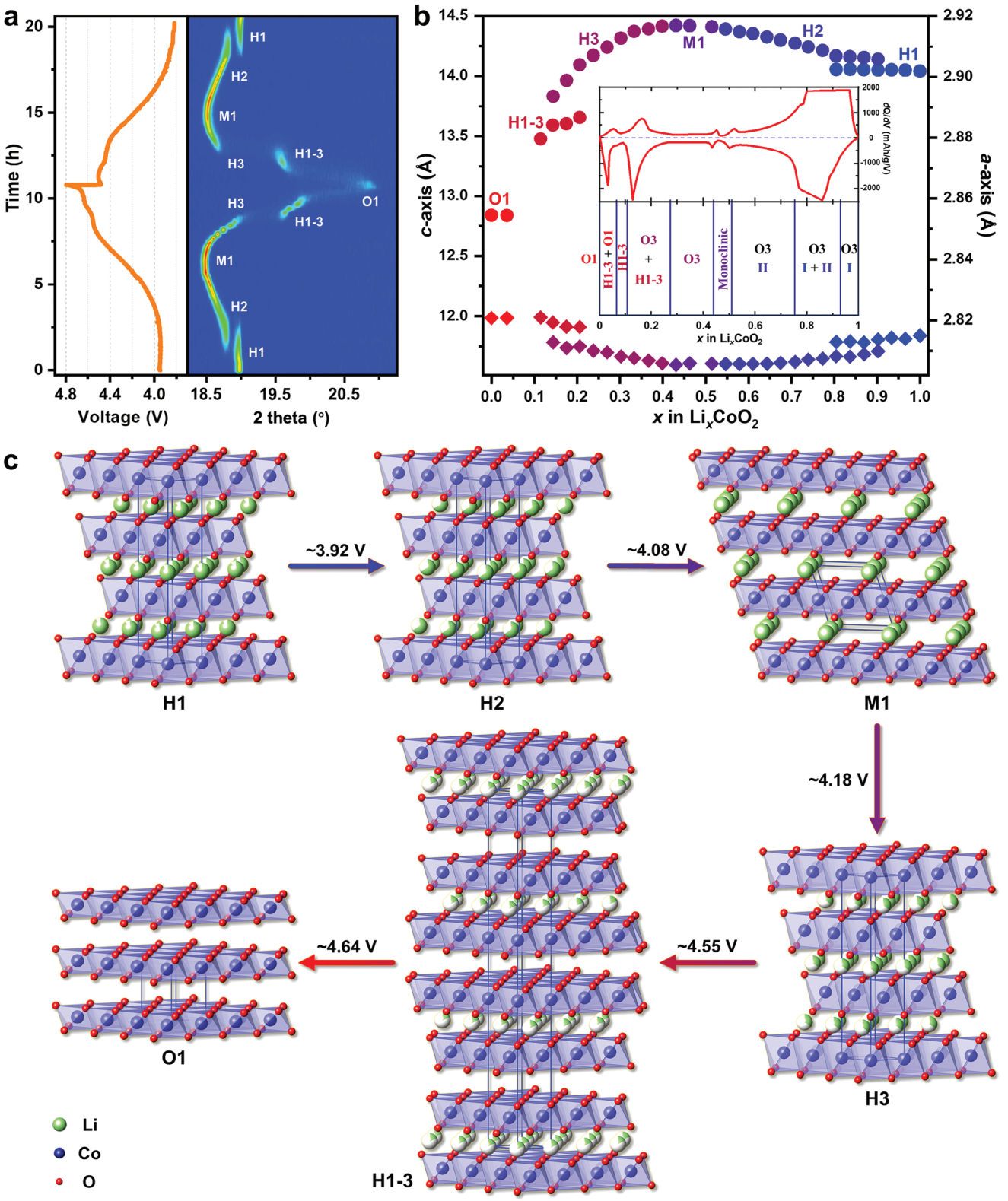

Figure 3. Phase evolution of LCO. a) In situ PXRD evolution of (003) peak with corresponding charge–discharge profile aligned to the left. Adapted with permission.[28] Copyright 2021, Springer Nature. b) Variation of *c*- and *a*-axis length in a hexagonal unit cell. Adapted with permission.[27b] Copyright 1996, The Electrochemical Society. Inset showing typical *dQ*/*dV* profile and phase diagram. Reproduced with permission.[29] Copyright 2004, Elsevier. c) Schematic phase evolution during charge.

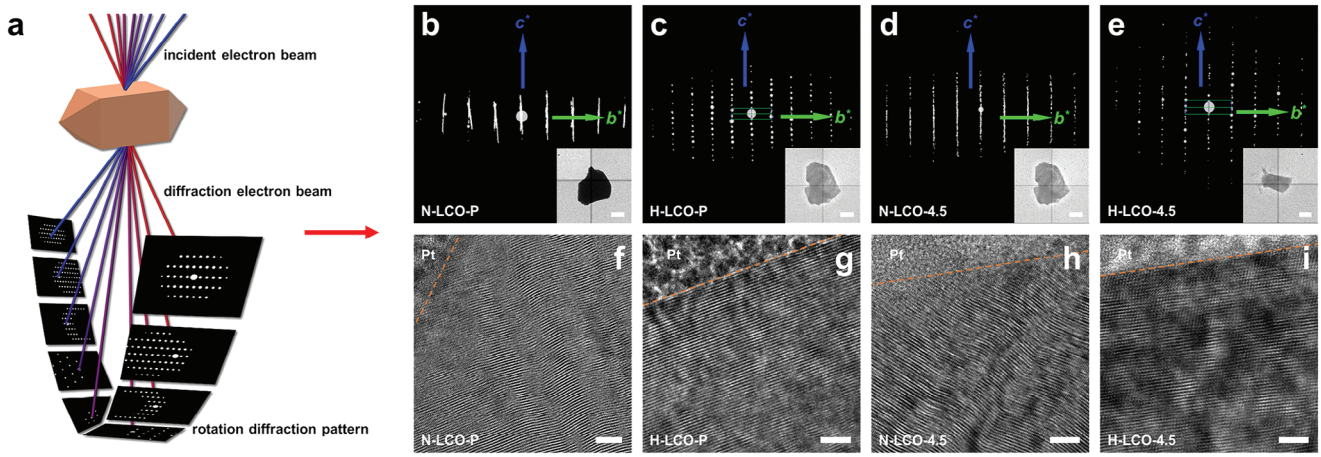

Figure 4. cRED schematic and combined cRED and HRTEM characterizations of N-LCO and H-LCO. a) Schematic data collection of cRED. b–e) Reconstructed 3D reciprocal lattice of N-LCO-P (b), H-LCO-P (c), N-LCO-4.5 (d), and H-LCO-4.5 (e) viewed along a^*-axis, with corresponding single particles as insets. f–i) HRTEM images of the near-surface region of N-LCO-P (f), H-LCO-P (g), N-LCO-4.5 (h), and H-LCO-4.5 (i) slices after FIB milling, with Pt deposited as surface protection. Suffix "P" and "4.5" denoting "pristine" and "charge to 4.5 V", respectively; scale bars: 500 nm for insets in b,e), 1 µm for insets in c,d), and 5 nm for f–i). Reproduced with permission.[28] Copyright 2021, Springer Nature.

severely degrades structural stability. Although Li^+ can be reinserted into the CoO_2 interlayer space of O1, seemingly potential in practice, the drastic structural changes make it unpractical, at least for now.

During discharge, LCO undergoes reverse phase transitions, but usually at lower voltages due to polarization. Typically, discharge to 3.0 V, the common lower cut-off voltage of LCO, allows Li^+ to fully occupy AM vacancies restoring the $LiCoO_2$ formula. However, a recent electron paramagnetic resonance study uncovered that LCO does not fully recover to its pristine state, suggesting more complex structural changes.[42] If applying a smaller discharge voltage like 1.0 V, as excess Li^+ is injected into the LCO lattice, gradual reduction of Co^{3+}, that is, $LiCoO_2 \rightarrow Li_{1+x}Co^{II}Co^{III}O_{2-y} \rightarrow Co + Li_2O$, occurs during initial discharge and conversion of $Co \leftrightarrow CoO \leftrightarrow Co_3O_4 \leftrightarrow Li_xCoO_y$ is enabled in subsequent cycles.[43] Despite a larger initial capacity, this low-voltage discharge is not practical due to severe structural strain with remarkable volume expansion and detrimental cathode-electrolyte side reactions.

3.1.2. Single-Particle Structure

For more precise electrochemistry, a micro-electrode technique was employed on LCO single particle and revealed that its electrochemical performance regarding capacity, impedance, rate capability, and Li^+ diffusion coefficient, is comparable to that of bulk.[44] However, early TEM and ED showed that even cycled at low 4.2 V, severe strain and stress, defects and dislocations, and occasional fracture were detected in LCO single particles, accompanied by an irreversible transition to spinel phase owing to octahedral defects and tetrahedral ordering.[37a,45] This means that electrochemically induced changes in LCO single-particle structure may differ evidently from those of bulk, so special care is needed when dealing with local structures.

Using 3D continuous rotation electron diffraction (cRED) combining high-resolution transmission electron microscopy (HRTEM), we investigated the single-particle structure of two commercial LCOs, that is, a normal LCO (N-LCO) and an H-LCO, at the atomistic level.[28] cRED has revealed various complex material structures but is less applied in LIBs (**Figure 4a**).[46] While these LCOs have essentially the same composition, particularly elemental dopants, and overall structure, in situ PXRD and electrochemical tests suggest that H-LCO structure is more stable, which is challenging to interpret by routine techniques. cRED is thus employed to probe more useful structural details at different charge voltages, including open-circuit voltage (OCV), 4.2, 4.5, 4.6, and 4.8 V. It is found from reconstructed 3D reciprocal lattice that N-LCO single particles always exhibit more streaked reflections rather than discrete and well-shaped ones along c^*-axis (Figure 4b,c) while opposite is true for H-LCO (Figure 4d,e). This strongly implies more structural disorder regarding CoO_2 layers in N-LCO. HRTEM with focused-ion beam (FIB) milling evidences this, as more curved lattice fringes corresponding to CoO_2 layers with structural curvature are visualized in N-LCO than H-LCO, especially in the vicinity of particle surface (Figure 4f–i). These directly indicate structural disorder and are consistent with cRED, demonstrating that curvature of CoO_2 layers is detrimental to structural stability, as backed up by further theoretical calculations. Hence, our single-particle study discloses that the flatness of CoO_2 layers, peculiarly in near-surface regions, is crucial for the high-voltage structural stability of LCO.

During electrochemical cycling, LCO bears diverse structural defects and its single particles are inhomogeneous in reactivity. For instance, Yu et al. identified SOC heterogeneity along with the formation, population, and evolution of inactive domains in LCO single particles.[47] They suggested that this heterogeneity is closely related to rate and a higher current is inclined to cause inhomogeneity in electrochemical reactions and Li^+ distribution. Besides, they revealed high structural uniformity of LCO single particles by scanning hard X-ray nano-diffraction, implying that structural rigidity weakens flexibility and is disadvantageous to electrochemical performance.[48] Recently, Rao et al. used an optical interferometric scattering microscope to track the

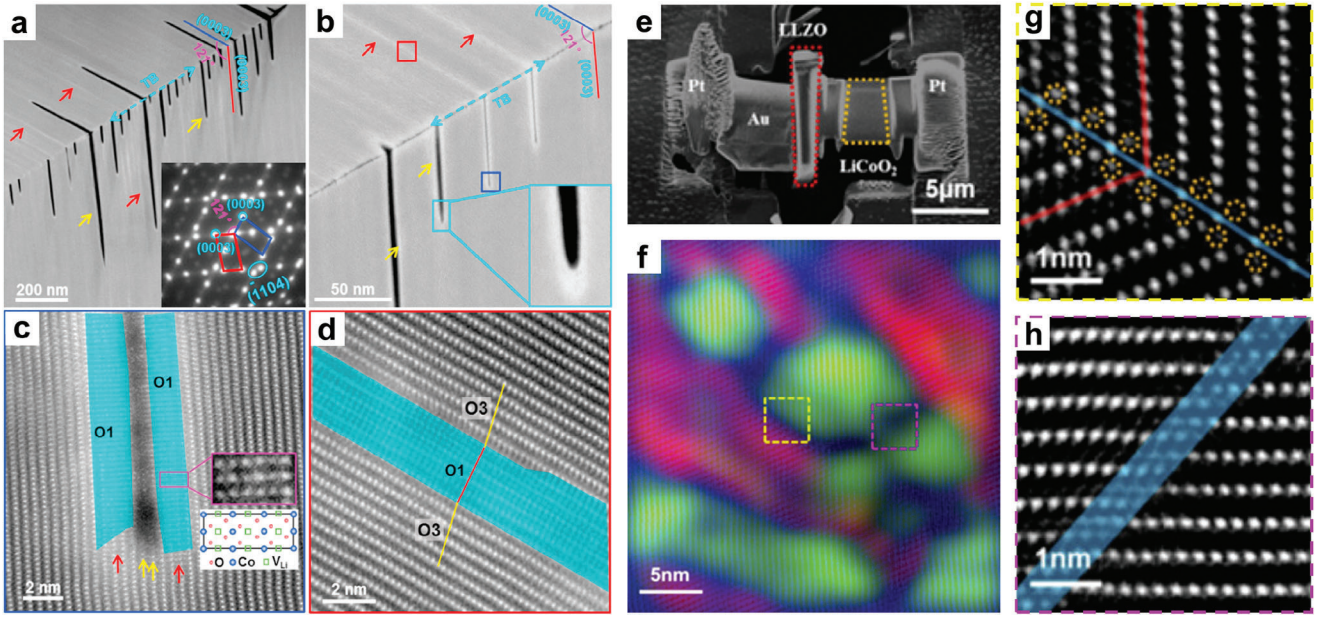

Figure 5. Twin boundary in LCO. a) Low magnification with corresponding ED pattern and b) enlarged HAADF-STEM images with red and yellow arrows indicating bright strips and cracks, respectively. c,d) HAADF-STEM images of blue (c) and red (d) area in b). Reproduced with permission.[49] Copyright 2020, Elsevier. e) Scanning electron microscopy (SEM) image of the micro-scale all-solid-state cell on nanochip. f) HAADF image of charged LCO colored by geographical phase analysis. g,h) HAADF-STEM images of yellow (g) and pink (h) area in f), with the constrast in AM layers showing Co presence. Reproduced with permission.[52] Copyright 2017, American Chemical Society.

nanoscale ion dynamics on an LCO single-particle matrix.[32b] Not only insulator–metal H1/H2 transition, H2 solid–solution evolution, disordering–ordering H2/M1 transition, and their Li^+ diffusion dynamics are visualized and quantified at the single-particle level, but more importantly the formation and destruction of M1 domains with varied orientations are captured in real time in a $Li_{0.5}CoO_2$ particle. These studies indicate the electrochemical heterogeneity in LCO single particles, which causes inhomogeneous delithiation and lithiation with segregation of phase and phase transition and aggravates structural instability with intensified strain and stress.

3.1.3. Twin Boundary

Twin boundary is very common even in pristine LCO particles, although they may appear as single crystals from the outside. Electron backscattered diffraction revealed that over 40% pristine LCO particles contain twin boundaries with an obvious trench on the surface.[49] Previous studies have identified two types of twin boundary in LCO: one is the coherent twin boundary with a 109.5° intersecting angle between two crystal basal planes and a small boundary energy of 0.3 J m^{-2}; the other is the antiphase domain boundary with exchanged AM and TM layers and a large boundary energy of 2.8 J m^{-2}.[50] However, their effects on LCO structural stability were not investigated in detail at that time. Recently, Sui et al. studied LCO twin boundaries during electrochemical cycles by atomic-resolved high-angle annular dark-field (HAADF) STEM.[49] Coherent twin boundary is found to act as an intrinsic planar defect that energetically favors not only cracks but also irreversible transition from O3 to O1 phase, accompanied by expansion of intersecting angle to larger ≈121° and void formation with lattice loss (**Figure** 5a–d). Two crack mechanisms are unveiled: deformation-type cleavage cracks with mechanical failure at low voltages (<4.4 V) and thermodynamic decomposition cracks as cracking nucleation mechanism upon high voltages (>4.4 V), which propagate into bulk lattice during long-term cycles and degrade LCO structural stability. Similar results are achieved in NCM811, showing that the twin boundary within "quasi-single-crystalline" particles aggravates irreversible phase transitions and capacity deterioration.[51] Accordingly, the twin boundary should be a preferred starting point for structural deformation and degradation, which needs caution and ought to be avoided as much as possible during synthesis.

Twin boundary also arises during the electrochemical process, possibly due to the release of structural stress. Using in situ STEM, Li et al. observed LCO structure in a micro-scale all-solid-state cell with Y- and Ta-doped LLZO ($Li_{6.75}La_{2.84}Y_{0.16}Zr_{1.75}Ta_{0.25}O_{12}$) SSE and Au anode (Figure 5e).[52] After charge to 2.1 V (vs Au; equal to 5.1 V vs Li/Li^+), pristine LCO single crystal fragments into numerous nanosized domains with abundant twin boundaries, including both coherent and antiphase ones with antisite Co (Figure 5f–h). Theoretical studies show that higher activation energy is required for Li^+ migration along and across these boundaries, affecting structural stability and rate capability.[50b] Recently, Kim et al. overcharged LCO to an extremely high 6.0 V and found a severe wedge-shaped twin boundary.[53] Not only uncommon corundum Co_2O_3 and spinel Co_3O_4 are revealed, but also lots of voids near twin boundaries with serious cation mixing. Hence, LCO structural degradation is attributed to phase heterogeneity and local SOC imbalance

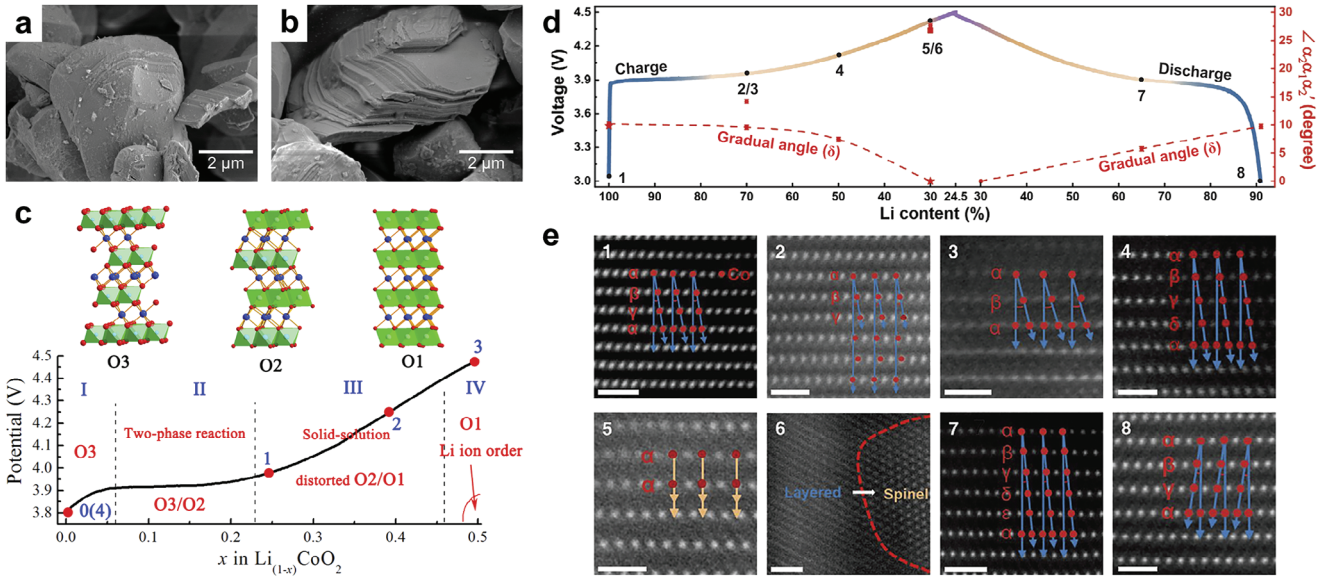

Figure 6. Layer gliding in LCO. a,b) Typical SEM images before (a) and after (b) cycling. Reproduced with permission.[55] Copyright 2018, American Chemical Society. c) Phase diagram correlating O3, O2, and O1. Reproduced with permission.[36a] Copyright 2012, American Chemical Society. d) Electrochemical profiles showing O3 (blue), O1 (orange), and rock-salt structure (purple) regions and gradual angles. e) HAADF-STEM images at corresponding states in d); scale bar: 1 nm. Reproduced with permission.[56] Copyright 2022, National Academy of Science.

induced by overcharge, emphasizing again the adverse electrochemical heterogeneity.

3.1.4. Layer Gliding

At high voltages, CoO_2 layers do not remain stationary but glide between each other. This is a spontaneous structural change that occurs as a result of the tendency to a more stable state with lower energy, although it is less stable than the pristine state. Early studies disclosed significant dislocations in individual LCO particles, forming the so-called single crystals rather than stacks of independent crystallites.[45,54] Macroscopically, these dislocations are reflected by the staircase-like morphology on the LCO particle surface, which is common and becomes pronounced after cycling (**Figure 6**a,b). This directly indicates the relative CoO_2 layer gliding along the basal plane, driven primarily by dissociation of a perfect dislocation into Shockley partial dislocations.[54] In addition, bulk phase transitions between O3, H1-3, and O1 are correlated with CoO_2 layer gliding, whose sluggish kinetics may be one of the causes for their poor reversibility.

With HAADF-STEM, Hu et al. achieved direct observation of CoO_2 layer gliding.[36a] Not only an O1 structure with ordered Li^+/vacancy at $x \approx 0.5$ ($Li_{0.5}CoO_2$) is found, but more importantly a new phase transition path from O3 to O2 then to O1 during charge to 4.5 V and from O1 back to O2 instead of O3 during discharge, showing irreversible CoO_2 layer gliding (Figure 6c). This first reports O2 in the phase transition of O3 LCO and associates previously unrelated structures. Recently, an in-depth investigation on the kinetic mechanism of CoO_2 layer gliding was conducted.[56] By introducing a gradual angle (δ) to quantify the gliding degree at various stages, a collective and quasi-continuous process for CoO_2 layer gliding is identified (Figure 6d,e), completely unlike conventional phase separation or solid–solution transition. Such gliding reveals a connection between CoO_2 layers, which allows delithiation to perceive Li^+ migration and rapidly respond to even a small change in Li^+ concentration with structural adjustment represented by the gradual angle. An O1 is found at $x = 0.3$ ($Li_{0.3}CoO_2$) and δ decreases from ≈9.847° in pristine O3 to nearly 0° in O1 and recovers during charge and discharge, respectively. Furthermore, new CoO_2 layer stacking patterns distinct from O3, H1-3, and O1 and local phase transition from O3 to O1 then to spinel and rock-salt phases are observed. These indicate that the local structure of CoO_2 layer gliding may undergo more complex variations than the bulk phase.

Upon higher 4.7 V, CoO_2 layer gliding occurs acutely and induces O3 to fully transform to O1. This variation in layer gliding causes substantial structural instability as it makes spinel phase transition easy to proceed even at low-temperature heating like 200 °C for 30 min.[57] Similar layer gliding has been explored in Ni-rich layered cathodes, implying its high correlation with intralayer TM migration and microstructural defects.[58] These suggest that suppressing oxygen vacancy may inhibit TMO_2 layer gliding and further irreversible phase transitions due to increased migration barrier.

3.2. Surface Structure

The surface is the termination of LCO bulk and directly contacts other LIB components like electrolytes and binders, governing Li^+ exit and entry and serving as a key in electrochemical performance. However, due to symmetry breaking with dangling bonds and exposure to external stimuli, LCO surface structure differs obviously from the bulk phase with inferior stability even at pristine state. For example, surface Co tends to occupy meta-stable

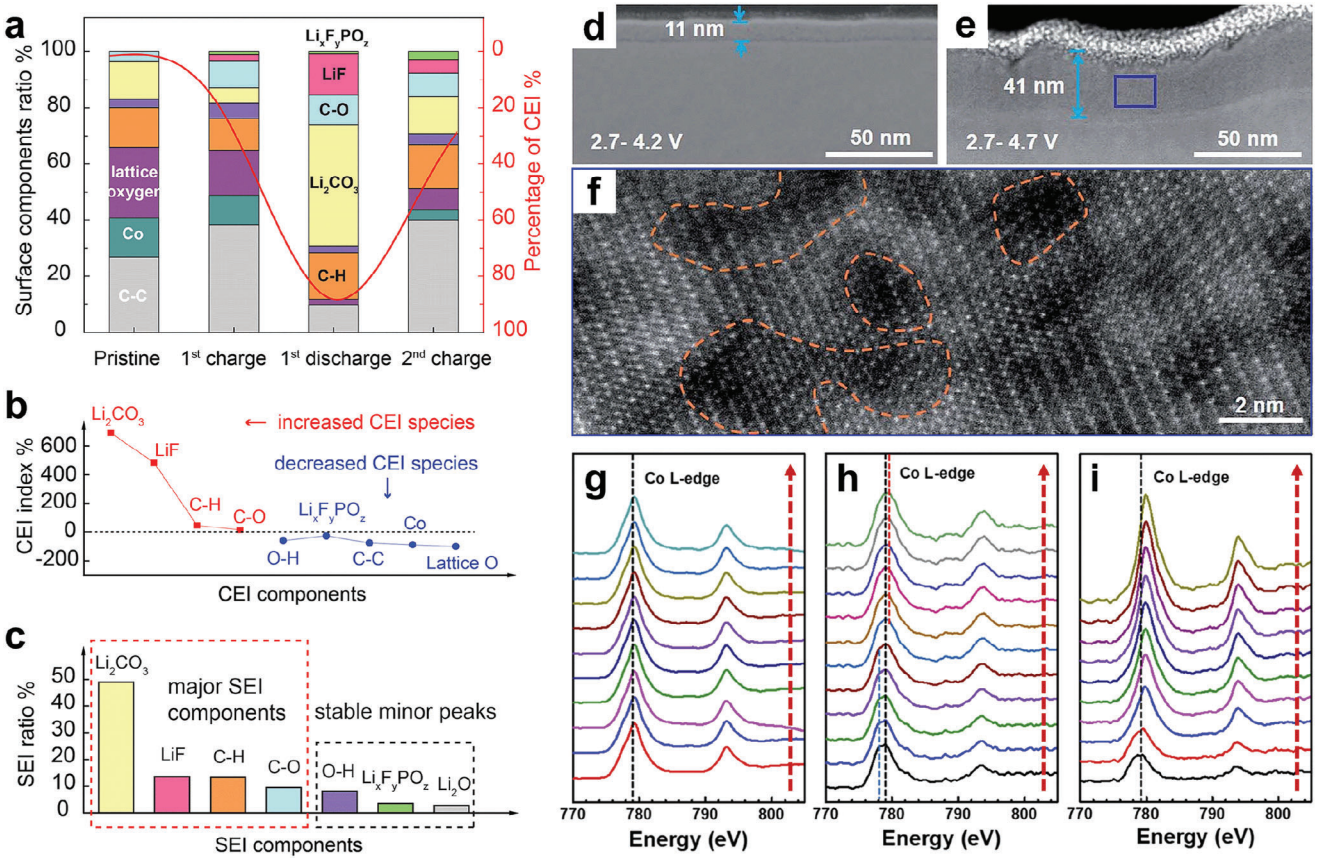

Figure 7. Interfacial side reactions on LCO. a) Dynamic CEI composition, with the species above the red curve considered as CEI components. b) CEI index of major components and c) corresponding SEI composition. Reproduced with permission.[61] Copyright 2018, Elsevier. d,e) TEM images of the surface degradation layer. f) HAADF-STEM image of blue area in e). Reproduced with permission.[57] Copyright 2019, The Royal Society of Chemistry. g–i) EELS spectra of Co L-edge at different states: pristine (g), charge to ≈4.18 V (h), and discharge to 3.0 V (i), with red dash arrow showing direction from surface to bulk. Reproduced with permission.[63] Copyright 2019, American Chemical Society.

tetrahedral interstices, leading to cobalt dissolution without cycling, and curved CoO_2 layers and structural distortion in the LCO surface have been visualized.[28,36a] Hence, the LCO surface is structurally unstable and undergoes more complex physicochemical processes during electrochemical cycles.

3.2.1. Interfacial Side Reaction

Interfacial side reactions between electrode and electrolyte occur inevitably and irreversibly, which change electrode surface structure and influence electrochemical behavior. Theoretically, if cathode potential lies below the highest occupied molecular orbital (HOMO) energy level of the electrolyte, oxidization of the latter by the former reacts at the cathode–electrolyte interface (CEI), forming the CEI film that prevents further contact and reactions. CEI on LCO surface was proposed by Goodenough et al. and validated later,[59] which grows thicker with increased temperature and cycles and is identified as a complex mixture. Currently, LCO CEI is widely recognized as a combination of inorganic (e.g., LiF, Li_2O, Li_2CO_3, $Li_xF_yPO_z$) and organic (e.g., carbonates, oligomers, polymers) components, similar to the solid electrolyte interface (SEI) on the anode. These species restrict the migration of Li^+ and/or electrons with enhanced interfacial impedance and can be tuned by electrolyte compositions and cycling conditions.

Atomic force microscopy indicated that CEI is a thin and loose film composed of fibrillar structures and inclined to form on an LCO edge plane rather than a basal one.[60] Using X-ray photoelectron spectroscopy, Li et al. carried out a thorough and quantitative study on dynamic CEI composition.[61] Surface species like CEI components and carbon additives vary obviously with electrochemical cycles (**Figure 7a**). A CEI index defined as (discharge ratio − charge ratio)/charge ratio × 100% is introduced to track its component change, revealing a strong correlation with SEI composition on Li anode and further an electrode interaction (Figure 7b,c). Although CEI thickens with increased cut-off voltages, it becomes unstable above 4.5 V and may decompose with long-term cycles. Kang et al. confirmed this, finding that the surface layer on LCO leaches out faster than accumulation upon charge to 4.8 V instead of less oxidative 4.6 V, which is considered as a "subtractive" modification for reducing polarization and unlike conventional "additive" surface modifications like coating.[62] Besides, it suggests that the structural instability of Li_xCoO_2 ($x < 0.5$) bulk may finitely affect cycling stability and partially explains why surface coating improves LCO high-voltage structural stability.

3.2.2. Phase Transition

During electrochemical cycles, structural rearrangements and irreversible phase transitions occur in the LCO surface with Co reduction, which are caused by cation defects (antisites and vacancies) and side reactions and propagate inside upon long-term cycles.[37a,64] For layered cathodes, the surface phase transition is more intense and complex and unlike that of bulk phase, readily follows a trend from layered to spinel and eventually to disordered rock-salt structure, which proceeds most gently in LCO but intensifies with increased voltages, temperature, and cycles.

Through HAADF-STEM, Sui et al. identified a degradation layer beneath CEI and composed of mainly spinel and voids in a cycled LCO surface, which monotonically thickens with improved voltages (Figure 7d–f).[57] Such a layer implies severe surface Li/Co antisites that result in irreversible phase transitions with deteriorated stability and stress release. Other studies using electron energy loss spectroscopy (EELS) reveal that after cycling, surface Co valence is lower than expected +3 and mixed phases like $LiCo_2O_4$, CoO, and Co_3O_4 are formed, accompanying nanocracks with Li^+ deficiency to accelerate structural degradation.[64,65] Moreover, Lu et al. screened the spatial gradient of surface Co valence following +2 to +3 and then to +4 from surface to bulk at both delithiation and end of discharge (Figure 7g–i).[63] This is ascribed to the interfacial side reactions of surface high-valent Co^{4+} reduction by electrolytes.

3.2.3. Cobalt Dissolution

LCO-electrolyte interfacial side reactions reduce oxidative Co^{4+} to Co^{2+}, which can leave the LCO surface to enter the electrolyte. This is cobalt dissolution, causing Co loss and further surface structural degradation. Besides, Co^{2+} can migrate to the anode, destroy SEI there, and eventually deposit on the anode surface. Tarascon et al. first quantified cobalt dissolution by analyzing the deposited cobalt species on the Li anode, suggesting that it is aggravated with increased voltages and cycles.[66] A direct correlation between cobalt dissolution and capacity loss was then established. Also, minor water contaminants in electrolytes and elevated temperatures can accelerate cobalt dissolution. As a result, not only active materials of LCO and electrolytes are lost, but also the surface structure of both electrodes is destroyed, thus exacerbating capacity and kinetics decay.

3.2.4. Oxygen Redox

Anionic redox of lattice oxygen is attracting wide interest, which is progressively involved in charge transfer upon deep delithiation and alters LCO structural stability. Theoretically, as charge proceeds in Li_xCoO_2 ($0.5 \leq x \leq 1.0$), electrons are extracted from Co 3*d*: t_{2g} orbitals, raising Co valence from +3 to +4, while the density of state remains almost unchanged with only a slight downward shift of Fermi level. As $x \leq 0.5$, electrons in the Co 3*d* orbitals top are nearly depleted and the Fermi level considerably shifts downward with the O 2*p* band top overlapping broadened Co 3*d* state. Hence, hybridization of Co 3*d* and O 2*p* states is enhanced and electrons start to transfer from O 2*p* to Co 3*d*: e_g orbitals for further delithiation with local O 2*p* holes produced.[67] This leads to oxidation of lattice oxygen with shortened O–O distance to even form peroxides or O_2, which evolves more drastically in the surface due to instable structure and outer stimuli. As a result, oxygen loss from Li_xCoO_2 ($x \leq 0.5$) can be further triggered to propel the compositions within the $LiCoO_2$-$Li_{0.5}CoO_2$-Co_3O_4 tie-line triangle in the Li–Co–O ternary phase diagram,[68] while resulting oxygen vacancies may also cause spin flip or even electron injection in nearby Co 3*d* electronic structure. Oxygen redox in LCO may be restrained by HS Co,[69] but various studies have shown that O, especially that in the surface, mainly and passively compensates for charge above 4.4 V.[63] Similar anionic redox is found in other layered oxides like LMRO and Li_2MnO_3 but is more severe.

Oxygen redox can be probed by resonance inelastic X-ray scattering (RIXS) technique. As the O K-edge RIXS spectra of LCO shown in **Figure 8a**, a well-defined shoulder appears at ≈523.5 eV emission energy upon deep charge, implying oxidization of lattice oxygen to higher valence ($O^{2-} \rightarrow O_2^{n-}$) with possible O—O bonding interaction.[70] This may further cause surface O_2 release resulting from bond breakage since Co—O bonding is too covalent to distort at high delithiation, which along with CO_2 from electrolyte oxidative decomposition can be detected by in situ differential electrochemical mass spectrometry (DEMS) (Figure 8b).[71] These suggest structural instability and safety risk of LCO surface, as high-valence O can not sustain at the particle surface and tend to release to destroy CEI film.[72] An in situ STEM and EELS study discovers that heating LCO surface after 4.6 V cycling also leads to O_2 production (Figure 8c), which is attributed to reduced O/Co ratio with surface voids and cracks formed (Figure 8d,e) and associates oxygen redox with Co migration and reduction facilitated by oxygen vacancies.[73]

Although oxygen redox evolution and its involvement in charge transfer remains poorly established, researches have revealed their close relation with LCO surface structure, including irreversible transitions with cobalt dissolution, exposed crystal facets and specific surface area, and interfacial side reactions.[57,75] Despite that oxygen redox is more pronounced in highly delithiated surfaces, this does not signify its absence in the LCO interior. An SCXRD study showed that minimum interlayer O–O distance shortens from 2.6180(9) Å in pristine $LiCoO_2$ to 2.5385(15) Å in $Li_{0.35}CoO_2$, indicating the participation of bulk lattice oxygen in charge compensation.[76] Recently, Yang et al. investigated LCO oxygen redox in depth.[74] By mapping of RIXS (mRIXS), distinct oxygen redox is revealed at 523.5 eV emission energy after 4.8 V charge (Figure 8f), which is derived from intraband excitation to the unoccupied O 2*p* final state. The neutron pair distribution function (NPDF) confirms this, as interlayer O–O distance decreases continuously during charge (Figure 8g). Nonetheless, theoretical calculations indicate that no O—O bonding interaction is formed even when deeply charged (Figure 8h). Hence, oxygen redox should occur globally in the LCO lattice and is disadvantageous to structural stability. On one hand, the ccp oxygen framework is the structural backbone and its changes reduce overall stability; on the other hand, oxygen redox allows electron injection from the HOMO energy level of electrolytes into O 2*p* band, causing electrolyte decomposition. And under other influences like interfacial side reactions and cobalt dissolution,

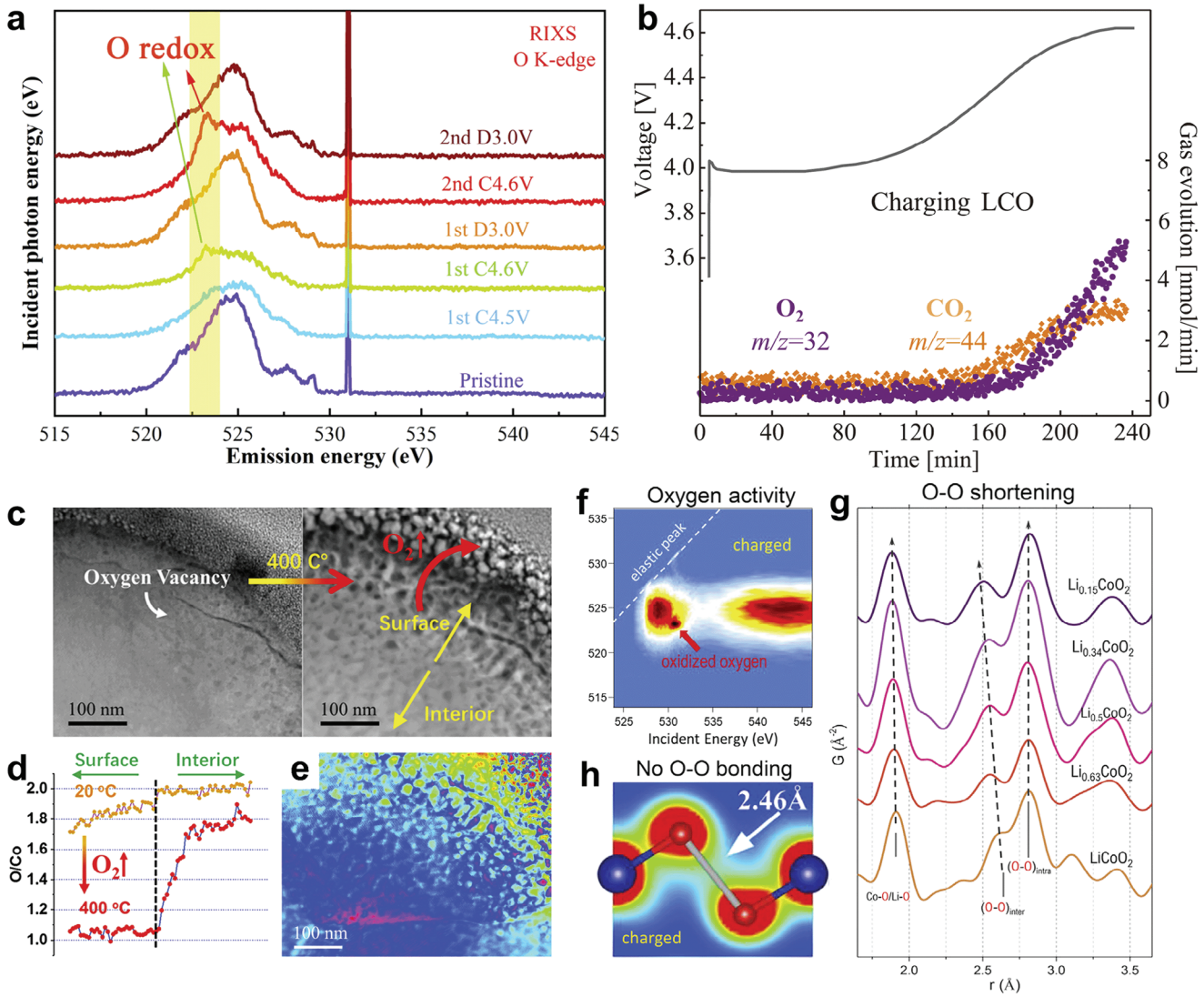

Figure 8. Oxygen redox in LCO. a) O K-edge RIXS spectra at various states. Reproduced with permission.[70] Copyright 2021, John Wiley & Sons, Inc. b) O_2 and CO_2 release detected by in situ DEMS. Reproduced with permission.[71] Copyright 2020, John Wiley & Sons, Inc. c) In situ STEM of heating cycled LCO surface. d) EELS-quantified O/Co ratio before and after heating. e) STEM image with the contrast showing surface nanovoids and cracks. Reproduced with permission.[73] Copyright 2020, American Chemical Society. f) O K-edge mRIXS after 4.8 V charge. g) Ex situ NPDF during charge. h) Sectional view of partial charge density in TM—O bonding energy range after charge. Reproduced with permission.[74] Copyright 2021, Elsevier.

such a process proceeds more vigorously in LCO surface, leading to structural destruction with O_2 release and phase transitions.

3.3. Structural Issue

Essentially, the high-voltage instability of LCO structure is attributed to the structural strain induced by Li^+ extraction and insertion chemistry, fundamentally the changes in ionic radii and electronic configurations of redox species, and in electrostatic interaction between CoO_2 layers. These processes are spontaneous and impossible to avoid, drive various structural variations and build-up stress, and ultimately destroy the LCO structure.

The structural stability of LCO bulk is mainly degraded by phase transitions beyond H3, namely H3/H1-3 and H1-3/O1, which are poorly reversible with significant anisotropic lattice strain and considered as a primary barrier for H-LCO. Specifically, the *c*-axis length drastically shortens by ≈5.3% from H3 to H1-3 and further by ≈5.9% upon O1, in contrast to ≈2.7% decrease over a larger *x* range from H1 to M1, while the *a*-axis length varies in the opposite direction, thus causing serious intraphase stress. These transitions are accompanied by sluggish CoO_2 layer gliding and inhomogeneous delithiation/lithiation to exacerbate stress. Worse still, sequential Li^+ extraction/insertion induces inexorably heterogeneity in not only Li^+ distribution but more crucially structures with interphase stress generated within individual particles. In addition, deleterious local strain like lattice curvature, dislocations, twin boundaries, as well as cobalt migration and oxygen redox, farther reduces structural reversibility. On the other hand, the inherent stiffness of LCO structure

is detrimental since Co—O bonding is so strongly covalent that it hardly yields to structural strain and distorts, making it difficult to reconcile structure and strain and unfavorable to stress release at high voltages. This leads to massive stress accumulation and is the driving force behind the formation of twin boundaries, cracks, and pulverization of LCO particles, which results in fresh surface structure exposed and readily damaged with a significant drop in elastic modulus, hardness, and fracture toughness.[77] Such structural instability is further intensified by long-term cycles and causes eventual bulk collapse with capacity decay.

Intrinsically unstable LCO surface changes more intricately and severely in electrochemical cycles to weaken high-voltage stability. Diverse surface variations, like interfacial side reactions, irreversible phase transitions, cobalt dissolution, and oxygen redox, are positively correlated and mutually reinforcing. For example, surface high-valence Co^{4+} and O_2^{n-} species from deep delithiation facilitate interfacial side reactions and catalyze CEI decomposition, which in turn promotes cobalt dissolution and oxygen redox. Migration and antisites of cation/vacancy are also boosted, leading to phase transitions and gas release as less oxygen is needed in resulting spinel and rock-salt structures. These processes repeat during cycling and undermine surface structure, notably upon high voltages, which not only expend active components but also impede interfacial Li^+ transport with increased impedance and capacity loss. Moreover, such structural changes attenuate the van der Waals force between LCO surface and other electrode ingredients, that is, binders like polyvinylidene difluoride (PVDF) and conductive agents like super P, causing contact failure that further impairs LCO surface structure.

Moreover, LCO structural stability is also subject to electrochemical factors besides voltage and cycling, especially to inhomogeneous electrochemistry. This is mainly ascribed to the varied orientations, distribution, and distances to the current collector of LCO particles, as well as to the non-uniform conductive network built by discontinuous conductive agents and binders.[78] These lead to polarization between and within individual particles and aggravate the already heterogeneous Li^+ extraction/insertion and phase distribution. Furthermore, a high rate amplifies such electrochemical and structural heterogeneity,[47] which accelerates strain/stress accumulation and deteriorates structural stability.

4. Structural Stabilization

Structural stabilization toward H-LCO should tackle two aspects, that is, bulk and surface structures, and corresponding strategies—elemental doping and surface modification—have been extensively studied with remarkable progress made in recent years. Despite direct contribution to respective bulk and surface, these strategies are not completely independent but closely related. Specifically, elemental dopants can enter the lattice, be enriched, or even form coatings on the LCO surface vicinity as surface modification, whereas the elements of surface coating can diffuse inside to act as subsurface doping. In the following, the stabilization of LCO is elaborated by modification strategies to further our structural understanding.

4.1. Elemental Doping

Elemental doping is most effective for stabilizing LCO bulk. Dopants can reside at Li^+, Co^{3+}, and O^{2-} sites depending on their own properties, particularly electronegativity and ionic radius, and tune LCO structure at the atomic scale, like defect concentration and distribution, cation rearrangement, charge redistribution, and electronic structure.[79] This endows benefits to strengthen structural stability, including suppression of irreversible phase transitions with alleviated strain/stress, mitigation of oxygen redox to stabilize anionic framework, expansion of interlayer spacing for enhanced Li^+ diffusion, and modulation of electronic structure with improved conductivity. However, the very low doping concentration in LCO (e.g., <0.5 wt.% in commercial applications) hinders the characterization of dopant homogeneity, form, and local structure and a deeper comprehension of its effect on structural stability. Despite massive elements used as LCO dopants so far, their roles are mostly derived qualitatively by comparing structures and performance before and after doping, thus not thoroughly understood. Not to mention that dopants slightly reduce capacity while the determination of the optimal doped element types, contents, and/or their combinations, doping strategies, synthetic techniques, etc., necessitates huge attempts and endeavors. Generally, foreign elements in the LCO lattice disrupt the original structural properties to a degree and affect strain behavior like CoO_2 layer gliding, phase transition, and oxygen redox, which is nevertheless beneficial to structural stabilization. Among numerous dopants, Ni, Ti, Mg, and Al are the most successful and well-studied with practicability.[13]

4.1.1. Single-Element Doping

Ni is the first dopant and expands the LCO lattice due to its larger ionic radius. While inducing particle polycrystallization, Ni not only reduces charge-transfer resistance but also suppresses unfavorable H1-3 and O1 phase transitions.[80] This is ascribed to Li/Ni antisites, a prevalent occurrence in Ni-rich cathodes because of similar Li^+ (0.74 Å) and Ni^{2+} (0.69 Å) ionic radii, allowing interlayer Ni (i.e., Ni in AM layers; $Ni_{AM\ layer}$ for short) to function as pillars with Ni—O bonding to support layered structure and inhibit CoO_2 layer gliding. DFT calculations confirmed this, revealing that the $Ni_{AM\ layer}$ is nearly immobile and that minor Li/Ni antisites do not obstruct Li^+ diffusion.[81] Meanwhile, attention should be paid to the Ni amount since excessive doping (e.g., 8%) may in turn deteriorate structural stability and Li^+ diffusivity. Moreover, a strong super exchange interaction through the O bridge is triggered between the antiferromagnetic $Ni^{2+}{}_{AM\ layer}$ ($3d^8$: $t_{2g}{}^6 d_z{}^2 d_{x^2-y^2}{}^1$) and open-shell ions in TM layers, that is, $Ni^{3+}{}_{TM\ layer}$ ($3d^7$: $t_{2g}{}^6 d_z{}^2 d_{x^2-y^2}{}^0$) and $Co^{4+}{}_{TM\ layer}$ ($3d^5$: $d_{xy}{}^2 d_{yz}{}^2 d_{xz}{}^1$) with unpaired electrons, which becomes stronger than that of $Ni^{2+}{}_{AM\ layer}$-O^{2-}-$Ni^{4+}{}_{TM\ layer}$/$Co^{3+}{}_{TM\ layer}$ during charge (**Figure 9a**).[82] Besides, such $Ni^{2+}{}_{AM\ layer}$-O^{2-}-$Ni^{3+}{}_{TM\ layer}$/$Co^{4+}{}_{TM\ layer}$ super exchange interaction reduces Co^{4+} to Co^{2+} through electron injection of $Ni^{2+}{}_{AM\ layer}$ while the $Ni_{AM\ layer}$ increases formation energy of oxygen vacancy,[83] hence stabilizing lattice oxygen by inhibiting valence oscillation and migration. Furthermore, Ni may induce a robust cationic mixed layer on the LCO surface to stabilize the surface structure.[84]

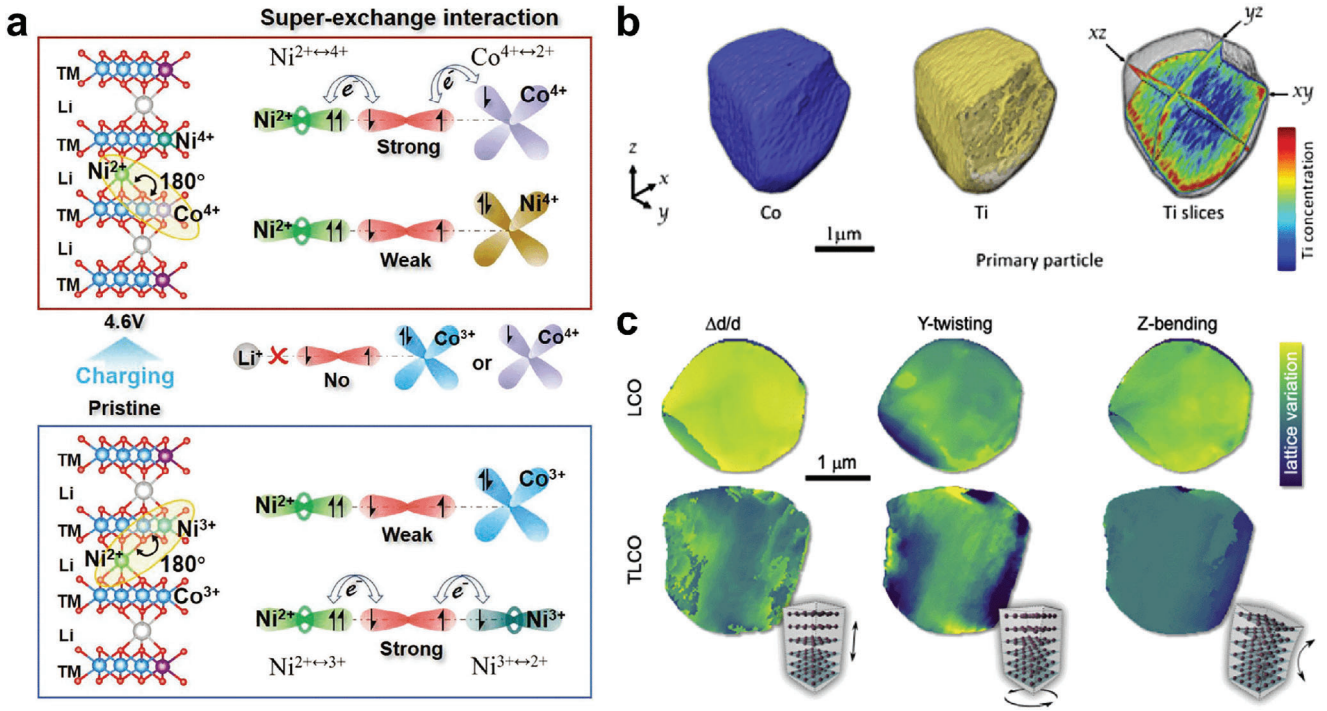

Figure 9. Ni and Ti doping in LCO. a) Super exchange interaction between $Ni^{2+}{}_{AM\ layer}$ and $TM_{TM\ layer}$ at pristine and charged (4.6 V) states. Reproduced with permission.[82] Copyright 2022, John Wiley & Sons, Inc. b) Nanofluorescence mapping of TLCO. c) Lattice distortion maps of bare LCO and TLCO. Reproduced with permission.[48] Copyright 2020, Elsevier.

Ti with +4 valence is another important TM dopant. Due to its poor solubility in LCO lattice, the theoretical maximum doping amount of Ti is 0.15%, and excess Ti tends to aggregate on LCO surface or even forms impurities.[85] Ti doping can enhance LCO structural and electrochemical stability with decreased particle dimension, while surface Ti restrains oxygen activity and stabilizes surface structure.[86] Recent DFT calculations manifested that Ti^{4+} doping at the Co^{3+} site induces Co^{2+}, resulting in lattice distortion and defects with improved conductivity.[87] Yu et al. conducted a further study by nanoresolution X-ray microscopy to probe the composition, valence, and lattice defects of Ti-doped LCO (TLCO).[48] It is disclosed that Ti heterogeneously and spontaneously segregates to modify particle surface and buried grain boundaries (Figure 9b). Besides, while bare LCO exhibits higher uniformity, more inhomogeneity in lattice deformation, including d-spacing heterogeneity (Δd/d), Y-twisting, and Z-bending, is found in TLCO (Figure 9c). These hierarchical defects mitigate intragranular stress, improve structural robustness, and hinder adverse H1-3 and O1 phase transitions.

Mg and Al are two representative non-TM dopants. Mg not only improves LCO structural stability but also facilitates Li^+ diffusivity and electronic conductivity from ≈10^{-3} to ≈0.5 S cm^{-1}, as attributed to Co^{4+} and holes induced by Mg^{2+} substituting Co^{3+} and shift of Fermi level to valence band with enhanced Co 3*d* and O 2*p* overlap.[88] Similar to Ni, Mg can also dope Li site owing to the comparable ionic radius (≈0.72 Å) to strengthen interlayer covalency with reduced Co 3*d* and O 2*p* hybridization. Huang et al. theoretically compared LCO with Mg doped at either Co (LCMO) or Li (LMCO) sites, showing that the latter is more stable because of lower formation energy.[89] An LMCO, that is, $Li_{0.9}Mg_{0.05}CoO_2$, was further synthesized, whose interlayer Mg is verified by STEM and synchrotron pair distribution function measurements. Such a Mg-pillaring effect prevents CoO_2 layer gliding and reduces the Li^+ migration barrier, thus helping suppress high-voltage phase transitions and interfacial side reactions. We recently advanced this study and discovered that Mg doping also induces bulk Li/Co antisites and a surface Mg—O layer, thereby preserving the stability of both the bulk and surface structure.[90] Furthermore, Liu et al. achieved LMCO and LCMO with the same 4% doping amount and confirmed the superior structural stability of LMCO, which is due to the above Mg-pillaring benefits plus alleviated CoO_6 distortion and structural stress.[91] Al as an LCO dopant also has various merits, such as 1) good lattice solubility due to similar ionic radius (0.535 Å) and same +3 valence as Co^{3+} and presence of isostructural λ-$LiAlO_2$, 2) excellent structural stabilization by stronger Al—O bonding (bond energy: 511 ± 3 kJ mol^{-1}) than Co—O (bond energy: 384.5 ± 13.4 kJ mol^{-1}) and invariable valence,[92] and 3) improved operating voltage and thermal stability. These confer LCO with not only increased OCV and Li^+ diffusivity but also hindered anisotropic lattice changes, two-phase behavior, M1 and H1-3 phase transitions, and cobalt dissolution. Besides, MAS NMR with others shows that Al may induce a surface lithiated spinel-like phase and a robust CEI layer to stabilize LCO surface structure.[93] However, Al may attract more lattice oxygen to be involved in charge compensation and excessive Al doping like 25% causes larger local distortion to degrade structural stability.[94]

Dopants can also act as growth mediators to alter the nucleation barrier and critical nuclei size by changing LCO surface energy.[95] Beside those, we recently revealed that contraction can

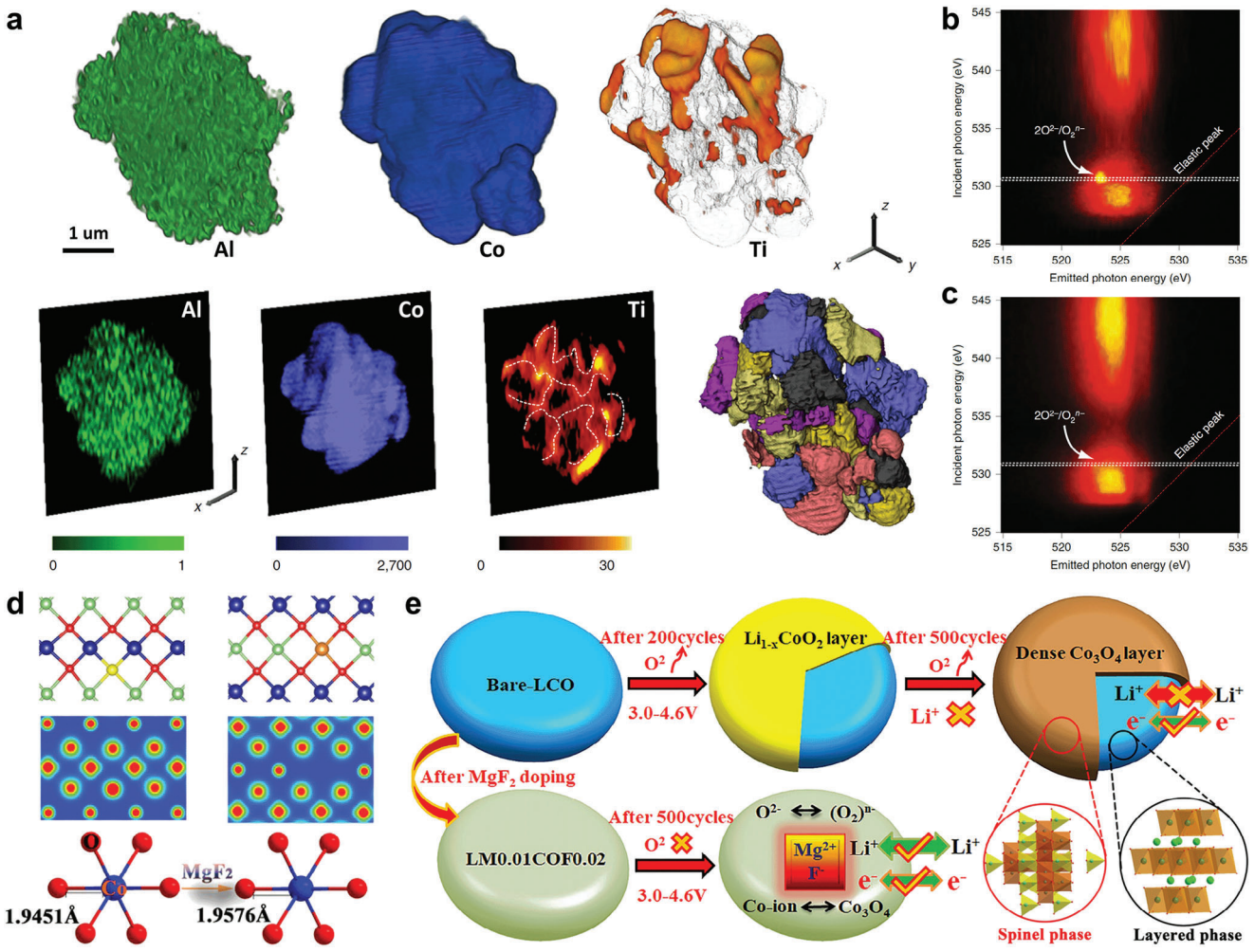

Figure 10. Multi-element co-doping for LCO. a) 3D elemental distribution (top level), typical 2D slice (down level), and identified and visualized sub-domain formation (lower right corner) of TMA-LCO. b,c) O K-edge mRIXS of bare LCO (b) and TMA-LCO (c) after charge to 4.6 V. Reproduced with permission.[86] Copyright 2019, Springer Nature. d) Electron distribution of oxygen and Co—O bond length and e) degradation mechanism before and after Mg—F co-doping. Reproduced with permission.[70] Copyright 2021, John Wiley & Sons, Inc.

stabilize LCO structure.[96] In addition to metals, non-metal elements have also been employed as dopants. F^- doping O^{2-} site, for example, increases ionic/electronic conductivity with stabilized lattice oxygen.[97] Moreover, F can dope or coat the LCO surface in fluoride form, serving as a conductive layer to lower interfacial impedance and prevent surface corrosion.

4.1.2. Multi-Element Co-Doping

Multi-element co-doping integrates the benefits of individual dopants to synergetically stabilize LCO structure and has been commercially applied with important progress. A representative example is La-Al co-doping, where the large La^{3+} ion ($r(La^{3+})$ = 1.032 Å) partly resides in AM layers as pillars to facilitate Li^+ diffusivity by widening interlayer spacing while Al^{3+} functions at the Co^{3+} site as positively charged center to disrupt M1 and H1-3 phase transitions, thereby alleviating lattice change and intragranular stress.[98] Li et al. advanced this stabilization with Ti-Mg-Al co-doping (TMA-LCO).[86] Through state-of-the-art synchrotron X-ray tomography with elemental analyses and STEM-EELS/energy-dispersive X-ray spectroscopy, dopant distribution is clearly demonstrated (**Figure 10a**). Mg and Al are bulk doping to enhance electronic conductivity and inhibit adverse phase transitions, whereas Ti is prone to segregate at grain boundaries to modify microstructure, which not only promotes uniform distribution of structural stress but also stabilizes surface structure by suppressing interfacial side reactions and oxygen activity (Figure 10b,c).

The distribution of co-doped elements can be altered by doping procedures. For instance, in TMA-LCO, Ti and Al can dope bulk phase to impede H1-3 transition while Mg can be surface gradient doping to protect surface structure.[99] This implies that dopant roles vary with distribution and that an interplay may exist amongst dopants. Our Ni-Ti-Mg co-doping work confirmed it, showing that Ni and Ti induce LCO polycrystallization and are enriched at grain boundaries while Mg causes inward migration of Ni and Ti as bulk dopants and itself is segregated at the

particle surface.[79] These enable solid links and buffers between neighboring particles, suppression of cleavage and cracks at grain boundaries, and further long-term structural stabilization.

Co-doping by metal and non-metal elements offers another excellent strategy, represented by Mg and F. Theoretical studies uncovered that Mg-F co-doping tailors LCO electronic structure by enlarging the energy gap between Co 3*d* and O 2*p* band centers with ρ increased from 0.3911 to 0.539 eV.[70] This alternation enhances Co—O bond ionicity with increased bond length and reduces electron distribution around oxygen (Figure 10d), hence inhibiting oxygen redox activity and improving cationic migration reversibility. Thanks to this, surface oxygen release and spinel Co_3O_4 formation are hindered to boost LCO structural stability (Figure 10e). Although several other combinations like Ca—P and Na—Fe have been investigated,[100] multi-element co-doping remains understudied with promising prospects.

4.2. Surface Modification

Surface modification aims specifically to stabilize the LCO surface to alleviate structural strain and issues induced by innate instability and external stimuli. Although dopants like Ni and Ti may be enriched on the LCO surface, the efficacy of element doping in such stabilization is limited. While varying with detailed strategies and mechanisms, surface modification for LCO can be broadly divided into two categories, that is, surface coating and modification of other components like electrolytes, additives, binders, and separators, with respective direct and indirect contributions to LCO surface.

4.2.1. Surface Coating

Surface coating basically constructs heterogeneous or solid–solution layers as physical barriers to protect surface structure, which may also promote charge transfer and reaction kinetics, act as HF scavengers to reduce electrolyte acidity, relieve structural deformation, and inhibit cobalt dissolution and oxygen release.[101] The function of surface coating is predominantly determined by the properties and morphologies of the coated materials. Despite being extensively studied, the surface coating still faces notable limitations regardless of its effectiveness. First, it may cause more capacity loss than elemental doping due to more non-active materials involved. Then, surface coating is commonly achieved through post-treatment rather than one-step synthesis, increasing complexity and cost. Additionally, the range of available coating materials is considerably broader compared to the limited types of doped elements. While this provides more possibilities, the trial-and-error workload and associated costs are significantly raised. For instance, an ideal coating should possess various qualities, like thinness and homogeneity, ionic and electronic conductivity, mechanical rigidity, ease of scalable processability, and cost-effectiveness,[102] and to develop coatings combining these properties is hence a formidable challenge. Moreover, for large-scale applications, other issues beyond cost also come into play, especially coating uniformity, stability, and efficiency. Based on responsiveness to electrochemical stimuli, surface coating roughly consists of electrochemically inert coating (by stable materials like Li-free oxides, fluorides, and phosphates) and electrochemically active coating (by materials such as Li-containing cathodes, SSEs, and conductive polymers).

Oxides with high thermodynamic and structural stability are the first to coat LCO. Al_2O_3 among them is the most successful, not only to inhibit surface structural changes like pitting corrosion, cobalt dissolution, and spinel transition but also to attenuate irreversible electrolyte decomposition and CEI growth.[64] However, oxide coatings are vulnerable to HF and convert to fluorides and harmful H_2O. More inert coatings are hence developed, especially fluorides and phosphates with stronger bonding to suppress interfacial side reactions and structural collapse with LiF formation. Though effective for stabilizing surfaces, the high energy barrier and lack of suitable binding sites in these coating structures lead to poor Li^+ conductivity and high electronic impedance, raising concerns on rate capability and capacity.

The coating may induce doping to further stabilize LCO surface structure. This is particularly evident in Al_2O_3 coating, as Al^{3+} can induce a $LiCo_{1-x}Al_xO_2$ solid–solution coating at 400 °C or entirely enter the LCO lattice as surface gradient doping at 800 °C.[103] Such is the presumed mechanism of Al-based coatings in preventing cobalt dissolution. Yang et al. employed such a coating strategy to achieve a $LiAlO_2/LiCo_{1-x}Al_xO_2$ dual coating by calcining Al_2O_3-coated LCO at specific 550 °C (**Figure 11a**).[104] These coatings play respective roles: inert $LiAlO_2$ protects the surface from electrolytes while subsurface $LiCo_{1-x}Al_xO_2$ acts as a structural transitional region and promotes Li^+ diffusion. Similar coating-induced doping is also found in MgO and $AlPO_4$ coatings. For MgO, Mg^{2+} can migrate to surface AM vacancies serving as pillars with strong Mg—O bonding, which hinders Co^{3+}/Co^{2+} redox and Li^+/vacancy ordering while causes a space charge layer to stabilize LCO-electrolyte interface (Figure 11b).[105] While $AlPO_4$ can lead to outmost P-rich coating (i.e., Li_3PO_4) and subsurface Al-rich doping (i.e., $LiCo_{1-x}Al_xO_2$) after calcination; these reduce electrolyte decomposition and induce Co- and Al-containing fluorides and/or oxyfluorides to restrain oxygen release and impedance growth.[106]

Coating-induced doping also occurs at anionic sites. A typical example is Se coating on commercial LCO (C-LCO), which substitutes some high-valent $O^{\alpha-}$ ($\alpha < 2$) in a deep-charged surface, forming a gradient Se doping with the outermost SeO_2 coating (Figure 11c).[71] Theoretical studies indicated that $Se^{\beta+}$ at O sites is unusual since Se is located out of the anion plane (Figure 11d). A selenite (SeO_3^{2-})-like resonant structure is suggested, whose Se valence varies with bonded O, for example, taking formal charge of $\beta = 4$ when O is 2- or lower valence ($0 < \beta < 4$) when O is oxidized. Such an "anti-aging" effect not only transplants pumped charges from $O^{\alpha-}$ to reduce it back to O^{2-} but also mitigates interfacial side reactions with stabilized redox of lattice oxygen and Co^{3+}/Co^{4+} (Figure 11e,f).

The electrochemically active coating has recently attracted attention owing to its additional benefits of promoted charge transfer and compensation. Li-containing phosphate ionic conductors are an effective active coating material. For example, even the simplest Li_3PO_4 coating can tune LCO-electrolyte interfacial decomposition while $Li_{1.4}Al_{0.4}Ti_{1.6}(PO_4)_3$ coating partly and exclusively converts to structurally coherent spinel and Li_3PO_4 after calcination, thus improving surface structural stability.[107] Yang et al. epitaxially grew $LiCoPO_4$ to fully cover and strongly bind

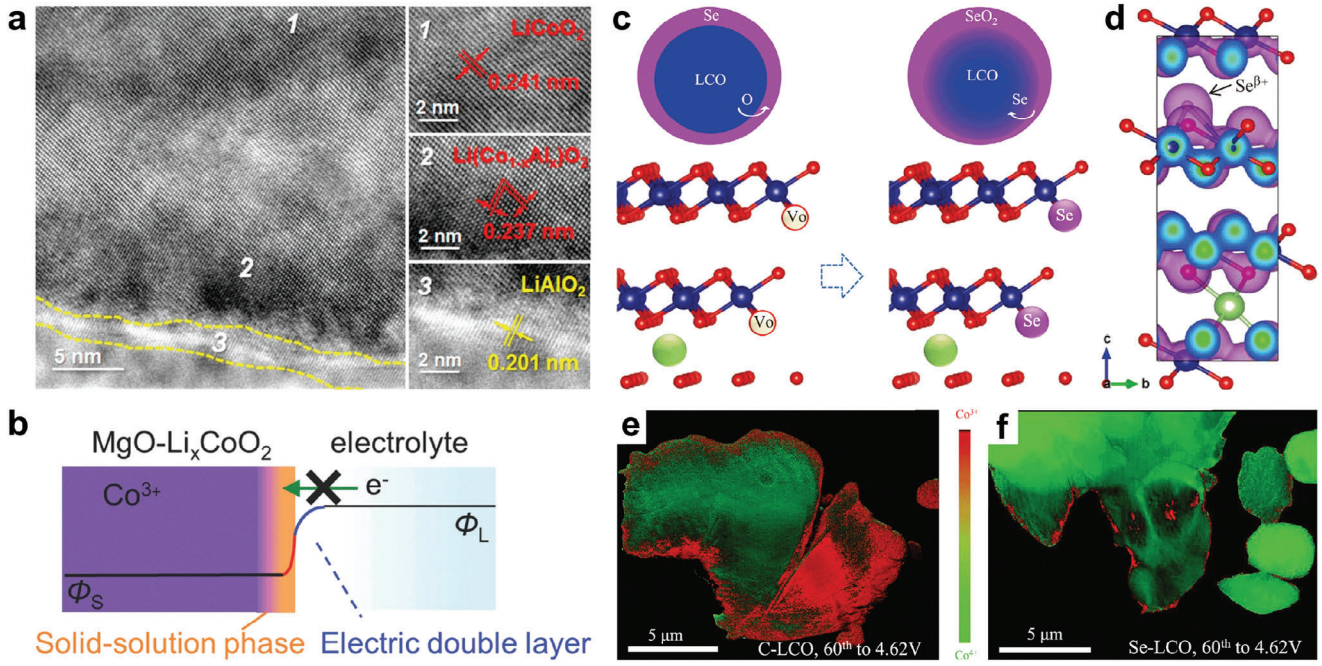

Figure 11. Electrochemically inert coating for LCO. a) HRTEM images of surface $LiAlO_2/LiCo_{1-x}Al_xO_2$ dual coating. Reproduced with permission.[104] Copyright 2019, Elsevier. b) Schematic electronic structure at MgO-coated LCO-electrolyte interface (ϕ_s and ϕ_L: electrochemical potentials of electrode and electrolyte). Reproduced with permission.[105] Copyright 2014, John Wiley & Sons, Inc. c) Schematic structure of Se substituting surface O during delithiation. d) Charge density distribution after Se doping. e,f) Co valence mapping of C-LCO (e) and Se-LCO (f) after 60th charge. Reproduced with permission.[71] Copyright 2020, John Wiley & Sons, Inc.

the LCO surface (LCPO-LCO).[108] Such a stable coating is well retained after long-term 4.6 V cycles and inhibits adverse nanovoids and irreversible spinel transition (**Figure** 12a,b). Moreover, the sound structural stability and interfacial compatibility with SSEs make these coatings ideal for all-solid-state LIBs.

Spinel-like materials offer another choice for active coatings due to their wide electrochemical window and less oxidized oxygen. A typical one is $LiMn_{0.75}Ni_{0.25}O_2$, which is lattice coherent on the LCO surface to suppress oxygen release by lowering the O 2*p* band top and enhance cationic and anionic redox reversibility.[110]

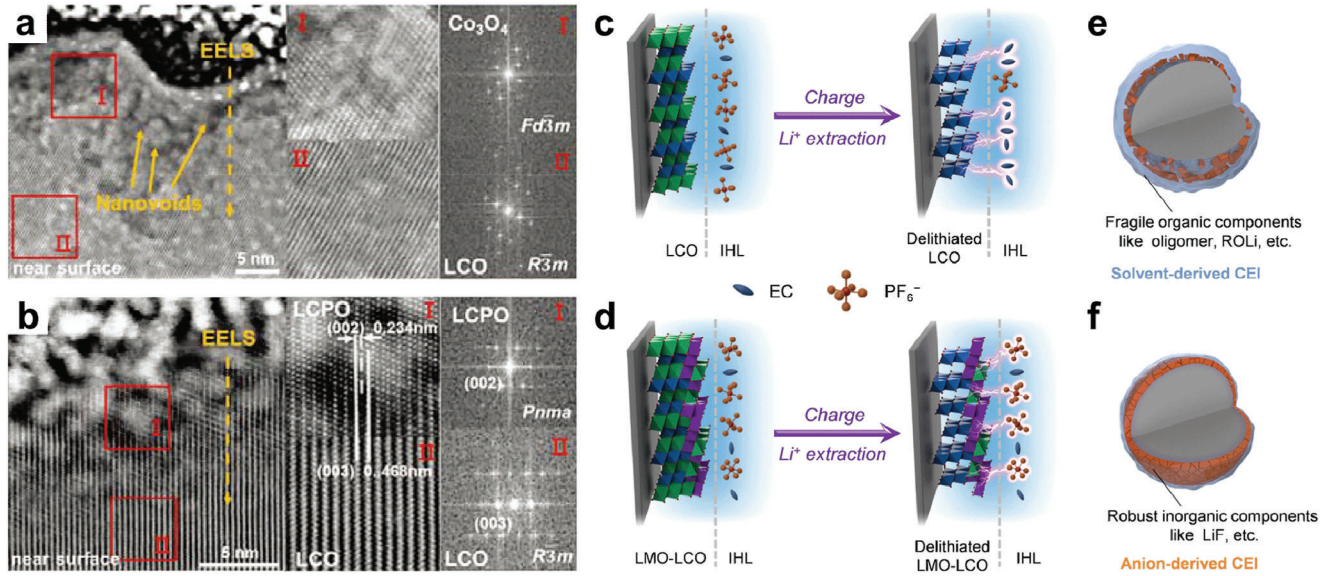

Figure 12. Electrochemically active coating for LCO. a,b) HAADF-STEM images with corresponding fast Fourier transform (FFT) patterns of bare LCO (a) and LCPO-LCO (b) after cycling. Reproduced with permission.[108] Copyright 2022, John Wiley & Sons, Inc. c–f) Schematic abundant species in IHL (c,d) and CEI (e,f) of bare LCO (c,e) and LMO-LCO (d,f). Reproduced with permission.[109] Copyright 2022, John Wiley & Sons, Inc.

We also achieved a spinel-like coherent coating via Al^{3+} and F^- dual gradients or Al^{3+}, F^-, and PO_4^{3-}co-modification to facilitate Li^+ diffusion kinetics and surface stabilization.[111] Further, Chen et al. showed that $Li_4Mn_5O_{12}$ spinel on LCO (LMO-LCO) enables an anion-rich inner Helmholtz layer (IHL) that prefers PF_6^- over ethyl carbonate (EC) (Figure 12c,d).[109] This causes inorganics (e.g., LiF) enriched in CEI to feature high modulus and mechanical robustness (Figure 12e,f) and modulates CEI composition. Besides those, rock-salt phases that boost surface conductivity and suppress near-surface structural destruction and perovskites that passivate and stabilize surface oxygen by enlarging η_{OER} (overpotential for oxygen evolution reaction),[68,112] are also effective active coating materials for LCO.

Aside from stabilizing the surface, coatings can improve LCO bulk stability, especially in suppressing phase transitions. Studies have shown that coatings may finitely impact low-voltage phase transitions like H2 and M1 but hamper high-voltage ones, that is, H1-3 and O1.[113] Although the mechanism for this is not clear, it may originate from two aspects: surface Li content alternation and coating-induced subsurface doping.[12] Also, we speculate that the bonding and wrapping effects of coating materials should obstruct CoO_2 layer gliding and resulting irreversible phase transitions, which occur at high voltages.

4.2.2. Modification of Other Components

Direct contact with other battery components allows LCO surface stabilization by modifications of these components, including electrolytes, additives, binders, and separators. This strategy is commonly achieved by constructing in situ an artificial protective layer on LCO. Though offering alternative optimization with wide interest, such modifications confront concerns besides cost, such as toxicity, stability, and concentration of electrolytes and additives, contact and conductivity of binders, and safety, thickness, and influence on rate capability of separators.

Conventional carbonate electrolytes usually have poor oxidative stability because they are susceptible to Co^{4+} and decompose at voltages below theoretical oxidation potentials. This promotes interfacial side reactions and destabilizes the LCO surface. Hence, modifications of electrolytes is necessary, which involve two topics. One is to explore innovative electrolytes with high-voltage stability, such as those based on sulfones and fluorinated carbonates. For instance, dimethly sulfone in a mixed solvent preferentially oxidizes to a stable protective layer on LCO to suppress cobalt dissolution and adverse side reactions.[114] The other is to modify conventional electrolytes by increasing Li salt concentration and adding additives. One representative is di(methylsulfonyl) ethane, whose high HOMO energy level makes it decompose prior to other solvents and polymerize to an artificial layer on both LCO and anode, thus reducing electrolyte decay and interfacial impedance.[115] Nitrile like 5-acetylthiophene-2-carbonitrile (ATCN), suberonitrile (SUN), and 1,3,6-hexanetricarbonitrile (HTCN), represents another class of effective additive.[116] Specifically, thiophene-based ACTN with C ≡ N and C═O groups not only undergoes electrochemically oxidization on LCO to induce a protective CEI layer but also employs its decomposed intermediates to convert harmful species, HF, H_2O, Li_2O, Li_2CO_3, and others, into a distinctive film comprising underneath compact Li salts and outer thiophene polymers. While SUN and HTCN possessing N 2*p* lone-pair electrons induce strong RCN^{δ}—$Co^{(4+\delta)+}$ bonding that lowers Co valence to prevent catalytic oxidation of electrolytes. Very recently, we reported that a lithium bisoxalatodifluorophosphate additive can create a bilayer composed of an outermost LiF-rich CEI layer and an inner spinel layer to efficiently protect the LCO surface.[117] By strong chelation with Co, a phytate lithium additive is also revealed to stabilize both LCO bulk and surface structure.[118]

Binders also affect LCO surface structure. Although PVDF is most widely used, it is not conducive as its van der Waals interaction with the LCO surface is weak, leading to issues such as inhomogeneous distribution and agglomeration causing polarization, and acceleration of Co_3O_4 formation and cobalt dissolution at the contacting points. This calls for binders with better performance, and examples like styrene-butadiene rubber-based latex binder and organosilicon-type binder have been developed, showing superior adhesion to LCO surfaces with higher flexibility and uniformity.[119] A dextran sulfate lithium (DSL) binder was lately found powerful via abundant hydrogen bonding.[120] It enhances surface Co—O bonding and structural stability by hindering electrolyte decomposition, cobalt dissolution, and H1-3 phase transition, while well retains after long-term cycles, in contrast to PVDF that barely impedes surface degradation (**Figure 13**).

Regarding separators, common polyethylene, and polypropylene contribute little to LCO surface stabilization, but their oxidative instability and thermal shrinkage instead affect LCO stability. Coating separators with gellable polymers and ceramics can improve ionic conductivity and adhesion between separators and LCO,[121] while composite separators benefit from reducing interfacial impedance. In addition, modifications of conductive agents can mitigate high-voltage side reactions to indirectly stabilize LCO surface structure.[122] Last but not least, blending with other cathodes like LFP may inhibit LCO particle breakage and surface Co_3O_4 formation, but its stabilization toward LCO surface structure is limited with uncertain mechanisms and at the expense of capacity.[123]

5. Conclusion and Outlook

Understanding LCO structure is a crucial and indispensable prerequisite for achieving H-LCO with higher capacity and energy density. This review exclusively highlights the LCO structure. Not only fundamentals of crystal and electronic structures but also various multi-scale structural instabilities occuring in bulk phase and surface are elucidated, which deepens our knowledge of LCO structure–performance relationship. It is concluded that LCO high-voltage stability is mainly subject to two aspects. One is poorly reversible H1-3 and O1 phase transitions in the bulk phase, causing significant anisotropic strain and stress to result in cracks and pulverization; the other is the dramatic changes in surface structure, inducing phase collapse with Co and O loss and crack propagation to LCO interior. To tackle these, targeted modifications with specific roles and mechanisms are elaborated from a structural perspective. It not only provides a comprehensive structural understanding but also helps the future effective and rational development of H-LCO with superior stability.

Despite considerable progress in LCO structural study, some issues remain barely understood. For bulk structure, neither the

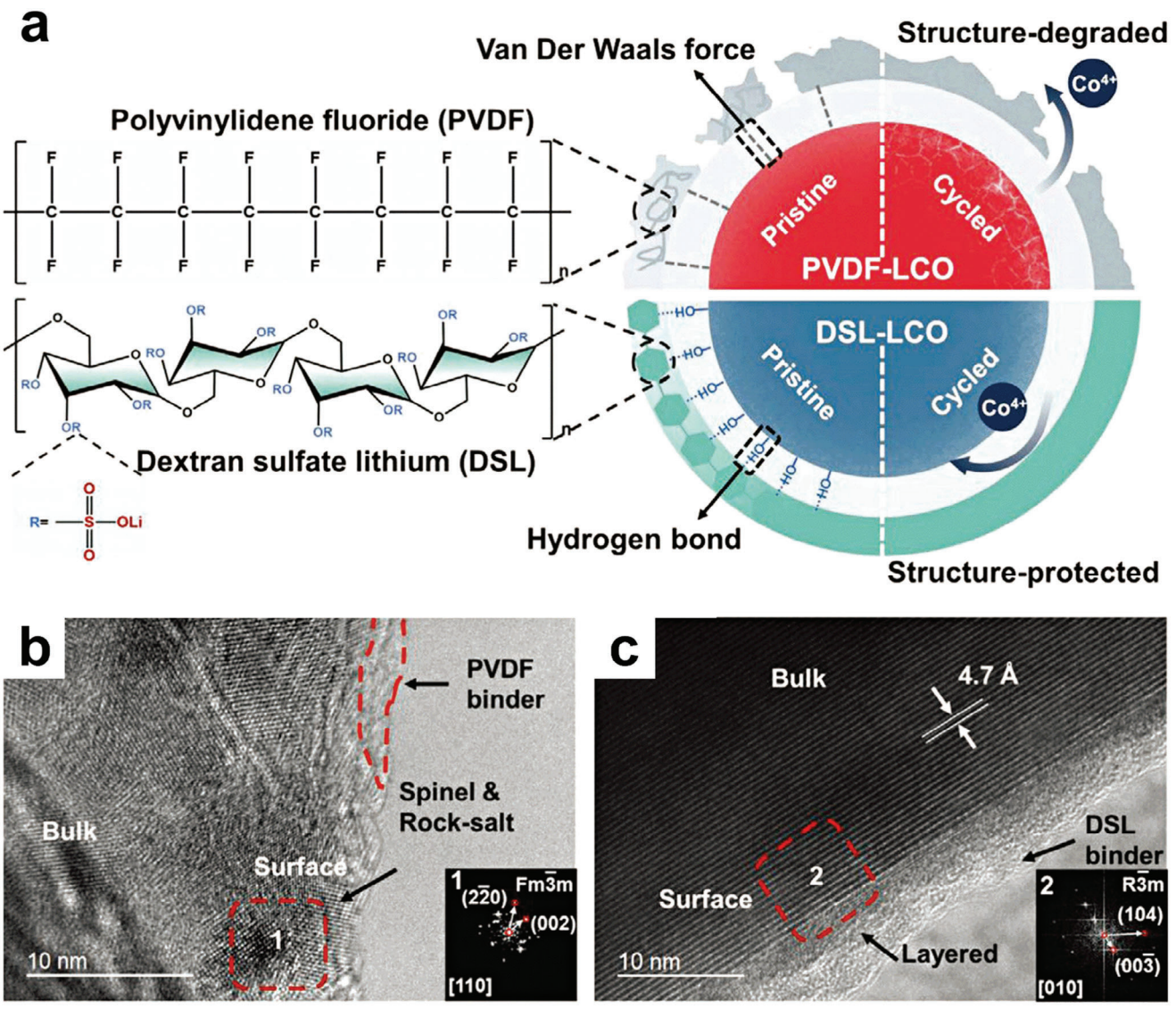

Figure 13. Modification of binder for LCO. a) Schematic interaction of PVDF and DSL binders with LCO surface. b,c) HRTEM and corresponding FFT images of LCO surface with PVDF (b) and DSL (c) binders after long-term 4.6 V cycles. Reproduced with permission.[120] Copyright 2021, John Wiley & Sons, Inc.

formation mechanism of H2a intermediate and O2- and O1-type structures at low voltages nor the selective segregation of Li^+ in every other AM layer in H1-3 and the driving force of CoO_2 layer gliding, are explicit. While for surface structure, quantification of various instabilities and their unambiguous relationship have not yet been explored. Besides, stabilization mechanisms of modifications, like dopant impacts on local crystal and electronic structures and concrete composition and structure of coatings and their interface with LCO, deserve more in-depth investigations.

Future structural understanding for high-voltage stabilization in H-LCO can be conducted in several ways: 1) combined use of state-of-the-art in situ*operando* characterizations to probe bulk and surface structures for more precise and complete structural and structure–performance knowledge; 2) employment of theoretical calculations based on a high-throughput machine/deep learning to predict and validate structure and performance, and further to guide modification strategies; 3) controllable synthesis of H-LCO with designed structural features, like specific defects, free of twin boundaries, dopants at particular positions, and specified surface/coating structures, morphologies, and orientations; 4) comprehensive structural stabilization by integrating elemental doping, surface coating, and modifications of other components. On all accounts, a solid and adequate structural understanding is the key foundation for LCO research and application, and there is still some way to go.

Acknowledgements

The authors acknowledge the financial support from the Basic and Applied Basic Research Foundation of Guangdong Province (No. 2021B1515130002), the Soft Science Research Project of Guangdong Province (No. 2017B030301013), the Shenzhen Science and

Technology Research Grant (No. ZDSYS201707281026184), the Hong Kong Research Grants Council (General Research Fund, No. 15221719), and the Guangdong Provincial Fund for Fundamental and Applied Research (No. 2021B1515130002).

Conflict of Interest

The authors declare no conflict of interest.

Keywords

lithium cobalt oxide, lithium-ion batteries, structural modifications, structural understandings, structure–performance relationship

Received: July 25, 2023
Revised: September 26, 2023
Published online: December 1, 2023

[1] D. Castelvecchi, E. Stoye, *Nature* **2019**, *574*, 308.
[2] W. Li, E. M. Erickson, A. Manthiram, *Nat. Energy* **2020**, *5*, 26.
[3] a) Y. Lyu, X. Wu, K. Wang, Z. Feng, T. Cheng, Y. Liu, M. Wang, R. Chen, L. Xu, J. Zhou, Y. Lu, B. Guo, *Adv. Energy Mater.* **2021**, *11*, 2000982; b) L. Wang, B. Chen, J. Ma, G. Cui, L. Chen, *Chem. Soc. Rev.* **2018**, *47*, 6505.
[4] K. Mizushima, P. C. Jones, P. J. Wiseman, J. B. Goodenough, *Mater. Res. Bull.* **1980**, *15*, 783.
[5] A. Manthiram, J. B. Goodenough, *Nat. Energy* **2021**, *6*, 323.
[6] A. Manthiram, *Nat. Commun.* **2020**, *11*, 1550.
[7] W. E. Gent, G. M. Busse, K. Z. House, *Nat. Energy* **2022**, *7*, 1132.
[8] J. Wu, P. Liu, Y.-S. Hu, H. Li, *Chuneng Kexue Yu Jishu* **2016**, *5*, 443.
[9] a) J. Zheng, S. Myeong, W. Cho, P. Yan, J. Xiao, C. Wang, J. Cho, J.-G. Zhang, *Adv. Energy Mater.* **2017**, *7*, 1601284; b) Q. Yang, J. Huang, Y. Li, Y. Wang, J. Qiu, J. Zhang, H. Yu, X. Yu, H. Li, L. Chen, *J. Power Sources* **2018**, *388*, 65.
[10] a) C.-W. Wang, S.-J. Zhang, C. Lin, S. Xue, Y.-P. Deng, B. Zhang, L. Yang, X. Yao, L. Zeng, J.-T. Li, F. Pan, Z.-W. Yin, *Nano Energy* **2023**, *108*, 108192; b) L. Feng, Z.-W. Yin, C.-W. Wang, Z. Li, S.-J. Zhang, P.-F. Zhang, Y.-P. Deng, F. Pan, B. Zhang, Z. Lin, *Adv. Funct. Mater.* **2023**, *33*, 2210744.
[11] https://www.webofscience.com/wos/woscc/basic-search (accessed: September 2023).
[12] K. Wang, J. Wan, Y. Xiang, J. Zhu, Q. Leng, M. Wang, L. Xu, Y. Yang, *J. Power Sources* **2020**, *460*, 228062.
[13] B. Chu, Y.-J. Guo, J.-L. Shi, Y.-X. Yin, T. Huang, H. Su, A. Yu, Y.-G. Guo, Y. Li, *J. Power Sources* **2022**, *544*, 231873.
[14] a) X. Wang, X. Wang, Y. Lu, *Ind. Eng. Chem. Res.* **2019**, *58*, 10119; b) S.-D. Zhang, M.-Y. Qi, S.-J. Guo, Y.-G. Sun, X.-X. Tan, P.-Z. Ma, J.-Y. Li, R.-Z. Yuan, A.-M. Cao, L.-J. Wan, *Small Methods* **2022**, *6*, 2200148.
[15] W. D. Johnston, R. R. Heikes, D. Sestrich, *J. Phys. Chem. Solids* **1958**, *7*, 1.
[16] C. Delmas, C. Fouassier, P. Hagenmuller, *Physica B+C* **1980**, *99*, 81.
[17] J. H. Yang, H. Kim, G. Ceder, *Molecules* **2021**, *26*, 3173.
[18] N. Yabuuchi, Y. Kawamoto, R. Hara, T. Ishigaki, A. Hoshikawa, M. Yonemura, T. Kamiyama, S. Komaba, *Inorg. Chem.* **2013**, *52*, 9131.
[19] E. Rossen, J. Reimers, J. Dahn, *Solid State Ionics* **1993**, *62*, 53.
[20] J. E. Huheey, E. A. Keiter, R. L. Keiter, O. K. Medhi, *Inorganic Chemistry: Principles of Structure and Reactivity*, Pearson Education India, New Delhi, India **2006**.
[21] W. T. Hong, M. Risch, K. A. Stoerzinger, A. Grimaud, J. Suntivich, Y. Shao-Horn, *Energy Environ. Sci.* **2015**, *8*, 1404.
[22] a) D. Ensling, G. Cherkashinin, S. Schmid, S. Bhuvaneswari, A. Thissen, W. Jaegermann, *Chem. Mater.* **2014**, *26*, 3948; b) M. K. Aydinol, A. F. Kohan, G. Ceder, K. Cho, J. Joannopoulos, *Phys. Rev. B* **1997**, *56*, 1354.
[23] R. L. DeKock, H. B. Gray, *Chemical Structure and Bonding*, University Science Books, Mill Valley, CA, USA **1989**.
[24] T. Okumura, Y. Yamaguchi, M. Shikano, H. Kobayashi, *J. Mater. Chem.* **2012**, *22*, 17340.
[25] a) J. T. Hertz, Q. Huang, T. Mcqueen, T. Klimczuk, J. W. G. Bos, L. Viciu, R. J. Cava, *Phys. Rev. B* **2008**, *77*, 075119; b) J. Van Elp, J. L. Wieland, H. Eskes, P. Kuiper, G. A. Sawatzky, F. M. F. de Groot, T. S. Turner, *Phys. Rev. B* **1991**, *44*, 60906103; c) E. J. Cheng, N. J. Taylor, J. Wolfenstine, J. Sakamoto, *J. Asian Ceram. Soc.* **2017**, *5*, 113.
[26] M. Li, J. Lu, *Science* **2020**, *367*, 979.
[27] a) J. N. Reimers, J. R. Dahn, *J. Electrochem. Soc.* **1992**, *139*, 2091; b) G. G. Amatucci, J. M. Tarascon, L. C. Klein, *J. Electrochem. Soc.* **1996**, *143*, 1114; c) T. Ohzuku, A. Ueda, *Solid State Ionics* **1994**, *69*, 201.
[28] J. Li, C. Lin, M. Weng, Y. Qiu, P. Chen, K. Yang, W. Huang, Y. Hong, J. Li, M. Zhang, C. Dong, W. Zhao, Z. Xu, X. Wang, K. Xu, J. Sun, F. Pan, *Nat. Nanotechnol.* **2021**, *16*, 599.
[29] Z. Chen, J. R. Dahn, *Electrochim. Acta* **2004**, *49*, 1079.
[30] T. Motohashi, Y. Sugimoto, Y. Masubuchi, T. Sasagawa, W. Koshibae, T. Tohyama, H. Yamauchi, S. Kikkawa, *Phys. Rev. B* **2011**, *83*, 195128.
[31] C. A. Marianetti, G. Kotliar, G. Ceder, *Nat. Mater.* **2004**, *3*, 627.
[32] a) E. Flores, N. Mozhzhukhina, U. Aschauer, E. J. Berg, *ACS Appl. Mater. Interfaces* **2021**, *13*, 22540; b) A. J. Merryweather, C. Schnedermann, Q. Jacquet, C. P. Grey, A. Rao, *Nature* **2021**, *594*, 522.
[33] K. Y. Chung, W.-S. Yoon, H. S. Lee, J. Mcbreen, X.-Q. Yang, S. H. Oh, W. H. Ryu, J. L. Lee, W. I. Cho, B. W. Cho, *J. Power Sources* **2006**, *163*, 185.
[34] T. Ohzuku, A. Ueda, *J. Electrochem. Soc.* **1994**, *141*, 2972.
[35] Y. Shao-Horn, S. Levasseur, F. Weill, C. Delmas, *J. Electrochem. Soc.* **2003**, *150*, A366.
[36] a) X. Lu, Y. Sun, Z. Jian, X. He, L. Gu, Y.-S. Hu, H. Li, Z. Wang, W. Chen, X. Duan, L. Chen, J. Maier, S. Tsukimoto, Y. Ikuhara, *Nano Lett.* **2012**, *12*, 6192; b) Y. Takahashi, N. Kijima, K. Tokiwa, T. Watanabe, J. Akimoto, *J. Phys.: Condens. Matter* **2007**, *19*, 436202.
[37] a) H. Wang, Y.-I. Jang, B. Huang, D. R. Sadoway, Y.-M. Chiang, *J. Electrochem. Soc.* **1999**, *146*, 473; b) C.-N. Li, J.-M. Yang, V. Krasnov, J. Arias, K.-W. Nieh, *Electrochem. Solid-State Lett.* **2008**, *11*, A81.
[38] X. Sun, X. Q. Yang, J. Mcbreen, Y. Gao, M. V. Yakovleva, X. K. Xing, M. L. Daroux, *J. Power Sources* **2001**, *97*, 274.
[39] A. Van Der Ven, M. K. Aydinol, G. Ceder, G. Kresse, J. Hafner, *Phys. Rev. B* **1998**, *58*, 2975.
[40] Z. Chen, Z. Lu, J. R. Dahn, *J. Electrochem. Soc.* **2002**, *149*, A1604.
[41] M. Duffiet, M. Blangero, P.-E. Cabelguen, C. Delmas, D. Carlier, *J. Phys. Chem. Lett.* **2018**, *9*, 5334.
[42] B. Hu, F. Geng, M. Shen, B. Hu, *Magn. Reson. Lett.* **2022**, *3*, 61.
[43] J. Shu, M. Shui, F. Huang, Y. Ren, Q. Wang, D. Xu, L. Hou, *J. Phys. Chem. C* **2010**, *114*, 3323.
[44] T. Saito, K. Nishikawa, T. Nakamura, S. Seki, *J. Phys. Chem. C* **2020**, *124*, 16758.
[45] H. Gabrisch, R. Yazami, B. Fultz, *J. Power Sources* **2003**, *119*, 674.
[46] a) J. Li, C. Lin, Y. Min, Y. Yuan, G. Li, S. Yang, P. Manuel, J. Lin, J. Sun, *J. Am. Chem. Soc.* **2019**, *141*, 4990; b) J. Li, C. Lin, T. Ma, J. Sun, *Nat. Commun.* **2022**, *13*, 4016; c) Q.-F. Lin, Z. R. Gao, C. Lin, S. Zhang, J. Chen, Z. Li, X. Liu, W. Fan, J. Li, X. Chen, M A. Camblor, F.-J. Chen, *Science* **2021**, *374*, 1605; d) H. Luo, C. Lin, Y.-E. You, X. Zhang, J. Li, L. Zhang, J. Sun, Z. Wei, J.-S. Hu, *Matter* **2023**, *6*, P3598.
[47] Y. Xu, E. Hu, K. Zhang, X. Wang, V. Borzenets, Z. Sun, P. Pianetta, X. Yu, Y. Liu, X.-Q. Yang, H. Li, *ACS Energy Lett.* **2017**, *2*, 1240.
[48] Y.-S. Hong, X. Huang, C. Wei, J. Wang, J.-N. Zhang, H. Yan, Y. S. Chu, P. Pianetta, R. Xiao, X. Yu, Y. Liu, H. Li, *Chem* **2020**, *6*, 2759.

[49] Y. Jiang, P. Yan, M. Yu, J. Li, H. Jiao, B. Zhou, M. Sui, *Nano Energy* **2020**, *78*, 105364.
[50] a) S. J. Zheng, C. A. J. Fisher, T. Hitosugi, A. Kumatani, S. Shiraki, Y. H. Ikuhara, A. Kuwabara, H. Moriwake, H. Oki, Y. Ikuhara, *Acta Mater.* **2013**, *61*, 7671; b) H. Moriwake, A. Kuwabara, C. A. J. Fisher, R. Huang, T. Hitosugi, Y. H. Ikuhara, H. Oki, Y. Ikuhara, *Adv. Mater.* **2013**, *25*, 618.
[51] R. Zhang, C. Wang, M. Ge, H. L. Xin, *Nano Lett.* **2022**, *22*, 3818.
[52] Y. Gong, J. Zhang, L. Jiang, J.-A. Shi, Q. Zhang, Z. Yang, D. Zou, J. Wang, X. Yu, R. Xiao, Y.-S. Hu, L. Gu, H. Li, L. Chen, *J. Am. Chem. Soc.* **2017**, *139*, 4274.
[53] J. Oh, S.-Y. Lee, H. Kim, J. Ryu, B. Gil, J. Lee, M. Kim, *Adv. Sci.* **2022**, *9*, 2203639.
[54] H. Gabrisch, R. Yazami, B. Fultz, *Electrochem. Solid-State Lett.* **2002**, *5*, A111.
[55] W. Zhang, F. H. Richter, S. P. Culver, T. Leichtweiss, J. G. Lozano, C. Dietrich, P. G. Bruce, W. G. Zeier, J. Janek, *ACS Appl. Mater. Interfaces* **2018**, *10*, 22226.
[56] S. Li, Y. Sun, A. Gao, Q. Zhang, X. Lu, X. Lu, *Proc. Natl. Acad. Sci. U. S. A.* **2022**, *119*, e2120060119.
[57] Y. Jiang, C. Qin, P. Yan, M. Sui, *J. Mater. Chem. A* **2019**, *7*, 20824.
[58] X.-H. Meng, T. Lin, H. Mao, J.-L. Shi, H. Sheng, Y.-G. Zou, M. Fan, K. Jiang, R.-J. Xiao, D. Xiao, L. Gu, L.-J. Wan, Y.-G. Guo, *J. Am. Chem. Soc.* **2022**, *144*, 11338.
[59] M. Thomas, P. Bruce, J. Goodenough, *Solid State Ionics* **1985**, *17*, 13.
[60] W. Lu, J. Zhang, J. Xu, X. Wu, L. Chen, *ACS Appl. Mater. Interfaces* **2017**, *9*, 19313.
[61] J.-N. Zhang, Q. Li, Y. Wang, J. Zheng, X. Yu, H. Li, *Energy Storage Mater.* **2018**, *14*, 1.
[62] W. M. Seong, K. Yoon, M. H. Lee, S.-K. Jung, K. Kang, *Nano Lett.* **2018**, *19*, 29.
[63] S. Li, K. Li, J. Zheng, Q. Zhang, B. Wei, X. Lu, *J. Phys. Chem. Lett.* **2019**, *10*, 7537.
[64] A. Yano, M. Shikano, A. Ueda, H. Sakaebe, Z. Ogumi, *J. Electrochem. Soc.* **2016**, *164*, A6116.
[65] J. Kikkawa, S. Terada, A. Gunji, T. Nagai, K. Kurashima, K. Kimoto, *J. Phys. Chem. C* **2015**, *119*, 15823.
[66] G. Amatucci, *Solid State Ionics* **1996**, *83*, 167.
[67] T. Shang, D. Xiao, F. Meng, X. Rong, A. Gao, T. Lin, Z. Tang, X. Liu, X. Li, Q. Zhang, Y. Wen, R. Xiao, X. Wang, D. Su, Y.-S. Hu, H. Li, Q. Yu, Z. Zhang, V. Petricek, L. Wu, L. Gu, J.-M. Zuo, Y. Zhu, C.-W. Nan, J. Zhu, *Nat. Commun.* **2022**, *13*, 5810.
[68] M. Cai, Y. Dong, M. Xie, W. Dong, C. Dong, P. Dai, H. Zhang, X. Wang, X. Sun, S. Zhang, M. Yoon, H. Xu, Y. Ge, J. Li, F. Huang, *Nat. Energy* **2023**, *8*, 159.
[69] J. Zhang, D. Wong, Q. Zhang, N. Zhang, C. Schulz, M. Bartkowiak, K. An, L. Gu, Z. Hu, X. Liu, *J. Am. Chem. Soc.* **2023**, *145*, 10208.
[70] W. Kong, J. Zhang, D. Wong, W. Yang, J. Yang, C. Schulz, X. Liu, *Angew. Chem., Int. Ed.* **2021**, *60*, 27102.
[71] Z. Zhu, H. Wang, Y. Li, R. Gao, X. Xiao, Q. Yu, C. Wang, I. Waluyo, J. Ding, A. Hunt, J. Li, *Adv. Mater.* **2020**, *32*, 2005182.
[72] Q. Li, Q. Liang, H. Zhang, S. Jiao, Z. Zhuo, J. Wang, Q. Li, J.-N. Zhang, X. Yu, *Angew. Chem., Int. Ed.* **2023**, *62*, e202215131.
[73] C. Sun, X. Liao, F. Xia, Y. Zhao, L. Zhang, S. Mu, S. Shi, Y. Li, H. Peng, G. Van Tendeloo, K. Zhao, J. Wu, *ACS Nano* **2020**, *14*, 6181.
[74] E. Hu, Q. Li, X. Wang, F. Meng, J. Liu, J.-N. Zhang, K. Page, W. Xu, L. Gu, R. Xiao, H. Li, X. Huang, L. Chen, W. Yang, X. Yu, X.-Q. Yang, *Joule* **2021**, *5*, 720.
[75] S. Sharifi-Asl, F. A. Soto, A. Nie, Y. Yuan, H. Asayesh-Ardakani, T. Foroozan, V. Yurkiv, B. Song, F. Mashayek, R. F. Klie, K. Amine, J. Lu, P. B. Balbuena, R. Shahbazian-Yassar, *Nano Lett.* **2017**, *17*, 2165.
[76] Y. Takahashi, N. Kijima, K. Dokko, M. Nishizawa, I. Uchida, J. Akimoto, *J. Solid State Chem.* **2007**, *180*, 313.
[77] J. G. Swallow, W. H. Woodford, F. P. Mcgrogan, N. Ferralis, Y.-M. Chiang, K. J. Van Vliet, *J. Electrochem. Soc.* **2014**, *161*, F3084.
[78] G. Sun, F.-D. Yu, M. Lu, Q. Zhu, Y. Jiang, Y. Mao, J. A. Mcleod, J. Maley, J. Wang, J. Zhou, Z. Wang, *Nat. Commun.* **2022**, *13*, 6464.
[79] S. Song, Y. Li, K. Yang, Z. Chen, J. Liu, R. Qi, Z. Li, C. Zuo, W. Zhao, N. Yang, M. Zhang, F. Pan, *J. Mater. Chem. A* **2021**, *9*, 5702.
[80] M. Hirooka, T. Sekiya, Y. Omomo, M. Yamada, H. Katayama, T. Okumura, Y. Yamada, K. Ariyoshi, *J. Power Sources* **2020**, *463*, 228127.
[81] J. Liang, D. Wu, M. Hu, Y. Tian, J. Wei, Z. Zhou, *Electrochim. Acta* **2014**, *146*, 784.
[82] N. Qin, Q. Gan, Z. Zhuang, Y. Wang, Y. Li, Z. Li, I. Hussain, C. Zeng, G. Liu, Y. Bai, K. Zhang, Z. Lu, *Adv. Energy Mater.* **2022**, *12*, 2201549.
[83] W. Huang, C. Lin, M. Zhang, S. Li, Z. Chen, W. Zhao, C. Zhu, Q. Zhao, H. Chen, F. Pan, *Adv. Energy Mater.* **2021**, *11*, 2102646.
[84] M. Yoon, Y. Dong, Y. Yoo, S. Myeong, J. Hwang, J. Kim, S.-H. Choi, J. Sung, S. J. Kang, J. Li, J. Cho, *Adv. Funct. Mater.* **2020**, *30*, 1907903.
[85] S. Kim, S. Choi, K. Lee, G. J. Yang, S. S. Lee, Y. Kim, *Phys. Chem. Chem. Phys.* **2017**, *19*, 4104.
[86] J.-N. Zhang, Q. Li, C. Ouyang, X. Yu, M. Ge, X. Huang, E. Hu, C. Ma, S. Li, R. Xiao, W. Yang, Y. Chu, Y. Liu, H. Yu, X.-Q. Yang, X. Huang, L. Chen, H. Li, *Nat. Energy* **2019**, *4*, 594.
[87] H. Xu, J. Zhu, X. Ke, H. He, H. Zhang, H. Li, *Phys. Status Solidi B* **2021**, *258*, 2000412.
[88] H. Tukamoto, A. R. West, *J. Electrochem. Soc.* **1997**, *144*, 3164.
[89] Y. Huang, Y. Zhu, H. Fu, M. Ou, C. Hu, S. Yu, Z. Hu, C.-T. Chen, G. Jiang, H. Gu, H. Lin, W. Luo, Y. Huang, *Angew. Chem., Int. Ed.* **2021**, *60*, 4682.
[90] H. Ren, W. Zhao, H. Yi, Z. Chen, H. Ji, Q. Jun, W. Ding, Z. Li, M. Shang, J. Fang, K. Li, M. Zhang, S. Li, Q. Zhao, F. Pan, *Adv. Funct. Mater.* **2023**, *33*, 2302622.
[91] W. Kong, D. Zhou, De Ning, W. Yang, D. Wong, J. Zhang, Q. Li, J. Yang, C. Schulz, X. Liu, *J. Electrochem. Soc.* **2021**, *168*, 030528.
[92] Y. Jin, P. Lin, C. H. Chen, *Solid State Ionics* **2006**, *177*, 317.
[93] F.-E. Er-Rami, M. Duffiet, S. Hinkle, J. Auvergniot, M. Blangero, P.-E. Cabelguen, K. Song, F. Weill, C. Delmas, D. Carlier, *Chem. Mater.* **2022**, *34*, 4384.
[94] W.-S. Yoon, K.-B. Kim, M.-G. Kim, M.-K. Lee, H.-J. Shin, J.-M. Lee, *J. Electrochem. Soc.* **2002**, *149*, A1305.
[95] X. Li, L. Zhou, H. Wang, D. Meng, G. Qian, Y. Wang, Y. He, Y. Wu, Z. Hong, Z.-F. Ma, L. Li, *J. Mater. Chem. A* **2021**, *9*, 19675.
[96] J. Xia, N. Zhang, Y. Yang, X. Chen, X. Wang, F. Pan, J. Yao, *Adv. Funct. Mater.* **2023**, *33*, 2212869.
[97] S. Mao, Z. Shen, W. Zhang, Q. Wu, Z. Wang, Y. Lu, *Adv. Sci.* **2022**, *9*, 2104841.
[98] Q. Liu, X. Su, D. Lei, Y. Qin, J. Wen, F. Guo, Y. A. Wu, Y. Rong, R. Kou, X. Xiao, F. Aguesse, J. Bareño, Y. Ren, W. Lu, Y. Li, *Nat. Energy* **2018**, *3*, 936.
[99] L. Wang, J. Ma, C. Wang, X. Yu, R. Liu, F. Jiang, X. Sun, A. Du, X. Zhou, G. Cui, *Adv. Sci.* **2019**, *6*, 1900355.
[100] a) Y. Yu, W. Kong, W. Yang, J. Yang, Y. Chai, X. Liu, *J. Phys. Chem. C* **2021**, *125*, 2364; b) P. Oh, J. Yun, J. H. Choi, G. Nam, S. Park, T. J. Embleton, M. Yoon, S. H Joo, S. H. Kim, H. Jang, H. Kim, M. G. Kim, S. K. Kwak, J. Cho, *Adv. Energy Mater.* **2023**, *13*, 2202237.
[101] Z. Chen, Y. Qin, K. Amine, Y.-K. Sun, *J. Mater. Chem.* **2010**, *20*, 7606.
[102] U. Nisar, N. Muralidharan, R. Essehli, R. Amin, I. Belharouak, *Energy Storage Mater.* **2021**, *38*, 309.
[103] B. Han, T. Paulauskas, B. Key, C. Peebles, J. S. Park, R. F. Klie, J. T. Vaughey, F. Dogan, *ACS Appl. Mater. Interfaces* **2017**, *9*, 14769.
[104] L. Shao, L. Zhou, L. Yang, C. Jia, C. Wang, S. Hu, X. Zeng, C. Yang, C. Huang, Y. Zhou, X. Xi, *Electrochim. Acta* **2019**, *297*, 742.
[105] Y. Orikasa, D. Takamatsu, K. Yamamoto, Y. Koyama, S. Mori, T. Masese, T. Mori, T. Minato, H. Tanida, T. Uruga, Z. Ogumi, Y. Uchimoto, *Adv. Mater. Interfaces* **2014**, *1*, 1400195.

[106] A. T. Appapillai, A. N. Mansour, J. Cho, Y. Shao-Horn, *Chem. Mater.* **2007**, *19*, 5748.
[107] Y. Wang, Q. Zhang, Z.-C. Xue, L. Yang, J. Wang, F. Meng, Q. Li, H. Pan, J.-N. Zhang, Z. Jiang, W. Yang, X. Yu, L. Gu, H. Li, *Adv. Energy Mater.* **2020**, *10*, 2001413.
[108] X. Yang, C. Wang, P. Yan, T. Jiao, J. Hao, Y. Jiang, F. Ren, W. Zhang, J. Zheng, Y. Cheng, X. Wang, W. Yang, J. Zhu, S. Pan, M. Lin, L. Zeng, Z. Gong, J. Li, Y. Yang, *Adv. Energy Mater.* **2022**, *12*, 2200197.
[109] J. Liu, J. Wang, Y. Ni, J. Liu, Y. Zhang, Y. Lu, Z. Yan, K. Zhang, Q. Zhao, F. Cheng, J. Chen, *Angew. Chem., Int. Ed.* **2022**, *61*, e202207000.
[110] Z. Zhu, D. Yu, Z. Shi, R. Gao, X. Xiao, I. Waluyo, M. Ge, Y. Dong, W. Xue, G. Xu, W.-K. Lee, A. Hunt, J. Li, *Energy Environ. Sci.* **2020**, *13*, 1865.
[111] a) W. Huang, Q. Zhao, M. Zhang, S. Xu, H. Xue, C. Zhu, J. Fang, W. Zhao, G. Ren, R. Qin, Q. Zhao, H. Chen, F. Pan, *Adv. Energy Mater.* **2022**, *12*, 2200813; b) Z. Li, H. Yi, H. Ren, J. Fang, Y. Du, W. Zhao, H. Chen, Q. Zhao, F. Pan, *Adv. Funct. Mater.* **2023**, 2307913.
[112] a) S. Xu, X. Tan, W. Ding, W. Ren, Q. Zhao, W. Huang, J. Liu, R. Qi, Y. Zhang, J. Yang, C. Zuo, H. Ji, H. Ren, B. Cao, H. Xue, Z. Gao, H. Yi, W. Zhao, Y. Xiao, Q. Zhao, M. Zhang, F. Pan, *Angew. Chem., Int. Ed.* **2023**, *62*, e202218595; b) X. Tan, Y. Zhang, S. Xu, P. Yang, T. Liu, D. Mao, J. Qiu, Z. Chen, Z. Lu, F. Pan, W. Chu, *Adv. Energy Mater.* **2023**, *13*, 2300147.
[113] P. Pang, Z. Wang, Y. Deng, J. Nan, Z. Xing, H. Li, *ACS Appl. Mater. Interfaces* **2020**, *12*, 27339.
[114] X. Kong, R. Zhou, J. Wang, J. Zhao, *ACS Appl. Energy Mater.* **2019**, *2*, 4683.
[115] X. Zheng, T. Huang, G. Fang, Y. Pan, Q. Li, M. Wu, *ACS Appl. Mater. Interfaces* **2019**, *11*, 36244.
[116] a) D. Ruan, M. Chen, X. Wen, S. Li, X. Zhou, Y. Che, J. Chen, W. Xiang, S. Li, H. Wang, X. Liu, W. Li, *Nano Energy* **2021**, *90*, 106535; b) X. Yang, M. Lin, G. Zheng, J. Wu, X. Wang, F. Ren, W. Zhang, Y. Liao, W. Zhao, Z. Zhang, N. Xu, W. Yang, Y. Yang, *Adv. Funct. Mater.* **2020**, *30*, 2004664.
[117] H. Zhang, Y. Huang, Y. Wang, L. Wang, Z. Song, H. Wang, C. Xu, X. Tian, S. Wang, J. Fang, W. Zhao, H. Cao, X. Yao, J. Yang, R. Tan, L. Yang, F. Pan, Y. Zhao, *Energy Storage Mater.* **2023**, *62*, 102951.
[118] F. Zhang, N. Qin, Y. Li, H. Guo, Q. Gan, C. Zeng, Z. Li, Z. Wang, R. Wang, G. Liu, S. Gu, H. Huang, Z. Yang, J. Wang, Y. Deng, Z. Lu, *Energy Environ. Sci.* **2023**, *16*, 4345.
[119] a) H. Isozumi, T. Horiba, K. Kubota, K. Hida, T. Matsuyama, S. Yasuno, S. Komaba, *J. Power Sources* **2020**, *468*, 228332; b) J. Ahn, H.-G. Im, Y. Lee, D. Lee, H. Jang, Y. Oh, K. Chung, T. Park, M.-K. Um, J. W. Yi, J. Kim, D. J. Kang, J.-K. Yoo, *Energy Storage Mater.* **2022**, *49*, 58.
[120] H. Huang, Z. Li, S. Gu, J. Bian, Y. Li, J. Chen, K. Liao, Q. Gan, Y. Wang, S. Wu, Z. Wang, W. Luo, R. Hao, Z. Wang, G. Wang, Z. Lu, *Adv. Energy Mater.* **2021**, *11*, 2101864.
[121] J.-A. Choi, S. H. Kim, D.-W. Kim, *J. Power Sources* **2010**, *195*, 6192.
[122] H. Zhang, L. Ben, H. Yu, W. Qi, W. Zhao, X. Huang, *Carbon* **2020**, *162*, 519.
[123] H. Zhang, X. Li, W. Liu, H. Yue, Z. Shi, Y. Yin, S. Yang, *J. Alloys Compd.* **2021**, *869*, 159188.

Cong Lin currently serves as an Assistant Professor (Research) in Department of Applied Biology and Chemical Technology at The Hong Kong Polytechnic University. He received his B.E. from Chongqing University in 2013, was a joint Chongqing University-Peking University Ph.D. from 2013 to 2018, and obtained his Ph.D. in 2018. He then worked as a Postdoctoral Researcher at Peking University Shenzhen Graduate School from 2018 to 2021 and as a PolyU Distinguished Postdoctoral Fellow at The Hong Kong Polytechnic University from 2021 to 2023. Dr. Lin has been dedicated to the comprehensive understanding of fundamental structures and their correlation with the performance of functional solids in applications across energy, catalysis, and separation through state-of-the-art techniques.

Zu-Wei Yin received his Ph.D. from Xiamen University in 2019 and was a joint Ph.D. student at Lawrence Berkeley National Lab between 2016 and 2019. He was a Postdoctoral Fellow and then Assistant Researcher at the School of Advanced Materials, Peking University Shenzhen Graduate School between 2019 and 2022. Currently, Dr. Yin is an Assistant Professor in the College of Energy at Xiamen University. His research interests mainly focus on energy storage materials, electrochemical mechanisms, and advanced characterization techniques, such as EQCM, TEM, XAS, etc.

Guohua Chen received his B.E. from Dalian University of Technology in 1984, M.E. and Ph.D. from McGill University in 1989 and 1994, respectively. He joined The Hong Kong University of Science and Technology in 1994, was promoted to Professor in 2008, and worked as the Head of the Department of Chemical and Biological Engineering during 2012–2016. He moved to The Hong Kong Polytechnic University in 2017 as a Chair Professor of Energy Conversion and Storage while concurrently served as an Associate Vice President (Research Support). He is currently Chair Professor and Dean of the School of Energy and Environment at the City University of Hong Kong. His main research areas include advanced electrode materials for energy storage, electrochemical technologies for energy and environmental applications, and drying of high-value products. He was elected as a Fellow of the Canadian Academy of Engineering in 2022.

Feng Pan is a Chair Professor of Peking University, VP of Peking University Shenzhen Graduate School, Founding Dean of the School of Advanced Materials, and Executive Editor of the *Chinese Journal of Structural Chemistry*. He obtained his B.S. from Peking University in 1985 and Ph.D. from the University of Strathclyde in 1994. Prof. Pan has long been committed to the fundamental studies of structural chemistry and its application in advanced materials, especially energy conversion-storage materials and devices. He has published over 360 peer-reviewed papers and received prestigious awards including Battery Division Technology Award in 2018 and China Electrochemical Contribution Award in 2021.